

Supplementary Information

Thomas F. Harrelson¹, Varuni Dantanarayana², Xiaoyu Xie³, Correy Koshnick⁴, Dingqi Nai¹, Ryan Fair⁵, Sean A. Nuñez⁶, Alan K. Thomas⁷, Tucker L. Murrey⁴, Michael A. Hickner⁶, John K. Grey⁷, John E. Anthony⁸, Enrique D. Gomez⁵, Alessandro Troisi², Roland Faller¹, and Adam J. Moulé^{1,2}

¹Department of Chemical Engineering, University of California - Davis, CA, USA

²Department of Chemistry, University of California - Davis, CA, USA

³Department of Chemistry, University of Liverpool, Liverpool, UK

⁴Department of Materials Science and Engineering, University of California - Davis, CA, USA

⁵Department of Chemical Engineering, Pennsylvania State University, University Park, PA, USA

⁶Department of Materials Science and Engineering, Pennsylvania State University, University Park, PA, USA

⁷Department of Chemistry & Chemical Biology, University of New Mexico, Albuquerque, NM, USA

⁸Department of Chemistry, University of Kentucky, Lexington, KY, USA

1 Materials

1.1 Synthesis, Crystallization, and Characterization of BTBTs

All reactions were performed in flame-dried glassware under positive pressure of nitrogen, unless otherwise noted. Air and moisture-sensitive liquids were transferred by syringe or canula. Organic solutions were concentrated by rotary evaporation (1-20 mm Hg) at ambient temperature, unless otherwise noted. All reagents were purchased commercially, and were used as received unless otherwise noted. Flash column chromatography was performed as described by Still et al. [1], employing silica gel (60 Å pore size, 32-63 μm , standard grade, Dynamic Adsorbents). Thin-layer chromatography was carried on the silica gel TLC (20 x 20 w/h, F-2543, 250 μm).

Prior to neutron measurements, synthesized materials were purified as described previously [2]. Briefly, concentrated solutions (ca. 75 mg/mL) in anhydrous toluene (99.99%, Sigma-Aldrich) were made at 50 °C, and further heated to 60 °C to ensure dissolution. Solutions were cooled to ca. 5 °C, and held for approximately five hours to induce crystallization. Crystals were recovered through filtering, and the final product is white/light yellow.

Proton nuclear magnetic resonance (¹H NMR) spectra were recorded at 25 °C. Proton chemical shifts are expressed in parts per million (ppm, δ scale), and are referenced to tetramethylsilane (TMS) or to the residual protium in the solvent (CHCl₃, 7.27 ppm; CD₂HOD, 1.73 ppm; DHO, 4.67 ppm; CD₂HCN, 1.97 ppm). Data are represented as follows: chemical shift, multiplicity (s = singlet, d = doublet, t = triplet, q = quartet, m = multiplet

and/or multiple resonances), integration, and coupling constant (J in hertz).

1.1.1 BTBT synthesis

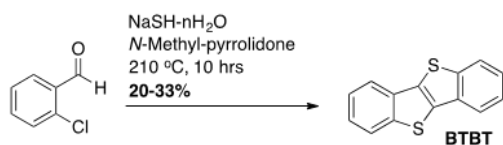


Figure S1: Reaction for BTBT synthesis.

We added 2-chlorobenzaldehyde (8.01 mL, 71.1 mmol, 1.0 equiv), and anhydrous N-methyl-2-pyrrolidone (NMP, 125 mL, 0.57 M) to a flame-dried flask under argon (Figure S1). The flask was capped with a septum, and the solution was degassed by bubbling argon for 25 min at room temperature. The flask was heated to 100 °C, and sodium hydrosulfide monohydrate was added to the solution (8.79 g, 156.4 mmol, 2.2 equiv). The reaction mixture was stirred for an additional 45 min at 100 °C, and then heated to 175 °C for 10 hours. The resulting product mixture was then cooled to room temperature, and poured into a solution of saturated ammonium chloride (400 mL). The resulting solution was extracted with toluene (3 extractions of 200 mL). The organics were then combined and washed with water (3 washes of 100 mL), followed by a wash with brine (100 mL) and dried over sodium sulfate. The product solution was filtered and evaporated under reduced pressure to yield a dark yellow residue. The product mixture was purified by recrystallization in acetone to yield BTBT single crystals. Consecutive recrystallizations from acetone/toluene were performed to increase purity. Chemical purity was determined by NMR spectroscopy (Figure S2).

1.1.2 m(acyl)-C7BTBT Synthesis

BTBT (1.0 g, 4.16 mmol, 1 equiv; synthesized using procedure above), anhydrous dichloromethane (100 mL, 0.042 M), and aluminum chloride (1.72 g, 12.9 mmol, 3.1 equiv) were added to a flame-dried flask

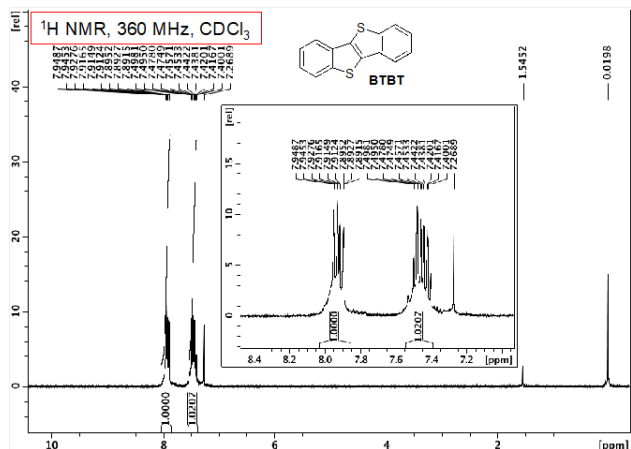


Figure S2: ¹H NMR (CDCl₃) δ : 7.89–7.95 (4H, m), 7.40–7.50 (4H, m).

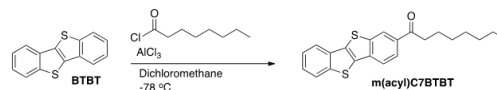


Figure S3: Reaction for m(acyl)-C7BTBT synthesis.

under argon (Figure S3). The flask was cooled to -78 °C, and octanoyl chloride was added dropwise (1 drop/second). The reaction mixture was stirred for an additional 2.5 hours at -78 °C. The resulting product mixture was poured into a beaker of crushed ice (50 mL), and 50 mL of saturated ammonium chloride was added to the beaker. The product mixture was poured into a separatory funnel, and extracted with dichloromethane (3 extractions of 100 mL). The organics were combined and washed with water, followed by a wash with brine, before being dried over sodium sulfate. The product was filtered, and the solvent evaporated under reduced pressure to yield a yellow residue. The product mixture was purified by recrystallization in toluene to yield m(acyl)-C7BTBT. Chemical purity was determined by NMR spectroscopy (Figure S4).

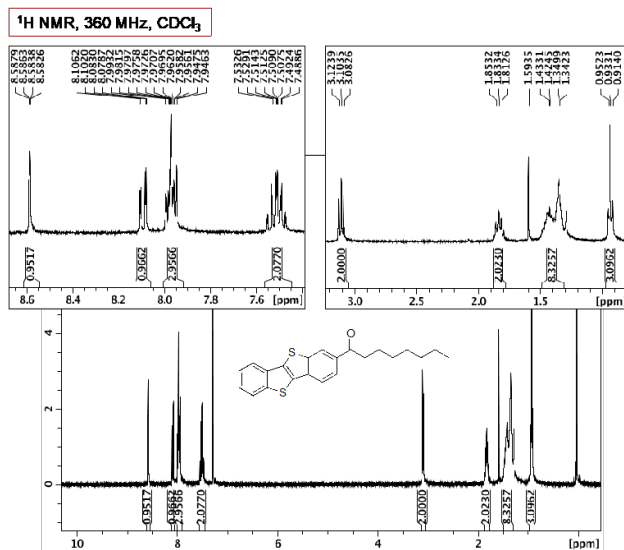


Figure S4: ^1H NMR (CDCl_3) δ : 8.58 (1H, bs), 8.09 (1H, dd, $J = 1.5$ Hz), 7.94–8.00 (3H, m), 7.46–7.55 (2H, m), 3.10 (2H, t, $J = 7.4$), 1.78–1.88 (2H, m), 1.30–1.50 (8H, m), 0.93 (3H, t, $J = 6.9$ Hz).

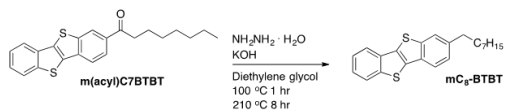


Figure S5: Reaction for *m8*-BTBT synthesis.

1.1.3 *m8*-BTBT Synthesis

M(acyl)-C7BTBT (1.0 g, 2.74 mmol, 1 equiv.), potassium hydroxide (0.42 g, 7.5 mmol, 2.25 equiv.), diethylene glycol (140 mL, 0.02 M), and hydrazine monohydrate (64–65% N_2H_4 , 2.18 mL, 35 mmol, 12.25 equiv.) was added to a flask (Figure S5). Then, the flask was immersed in an oil bath, and kept at 100 °C for 1 hour, then the temperature was increased to 210 °C for 8 hours. The resulting product mixture was then cooled to room temperature, and poured into water (200 mL) to precipitate the crude product. The precipitate was collected by filtration, and washed with methanol and water. The crude

solid product was dissolved in a minimum amount of 1:1 mixture of dichloromethane/toluene, then loaded onto silica, and eluted with hexanes. The product solution was then evaporated under reduced pressure to yield the *m8*-BTBT crystals. Chemical purity was determined by NMR spectroscopy (Figure ??).

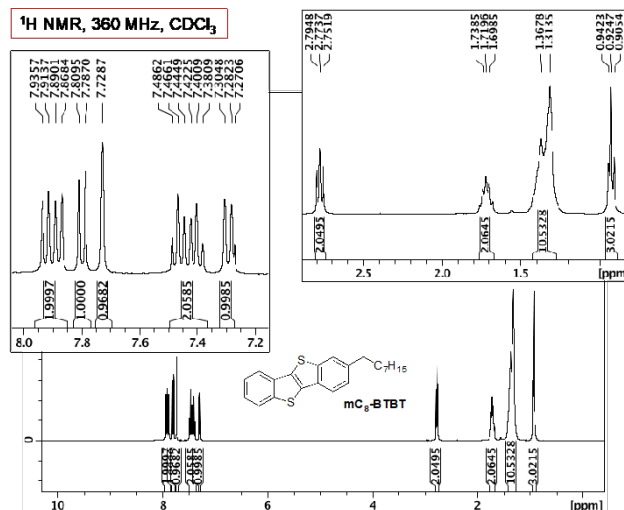


Figure S6: ^1H NMR (CDCl_3) δ : 7.91 (1H, d, $J = 7.9$), 7.86 (1H, d, $J = 7.8$ Hz), 7.78 (1H, d, $J = 7.9$ Hz), 7.72 (1H, s), 7.37–7.50 (2H, m), 7.28 (1H, d, $J = 8.1$ Hz), 2.77 (2H, t, $J = 7.6$ Hz), 1.66–1.77 (2H, m), 1.24–1.44 (10H, m), 0.92 (3H, t, $J = 6.3$ Hz).

1.1.4 (acyl)-C7-BTBT Synthesis

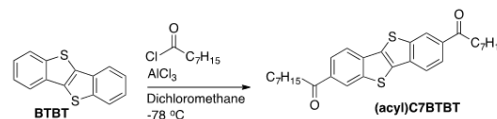


Figure S7: Reaction for (acyl)-C7-BTBT synthesis.

BTBT (0.2 g, 0.83 mmol, 1 equiv.), aluminum chloride (0.61 g, 4.6 mmol, 5.5 equiv.) and anhydrous dichloromethane (2 mL, 0.4 M) was added to a flame dried flask (Figure S7). The mixture was cooled to

-78 °C, and octanoyl chloride was added dropwise. The reaction mixture was stirred for 1 hour at -78 °C followed by an additional stirring period of 48 hours at room temperature. The product mixture was cooled to 0 °C and quenched with the addition of crushed ice. The product mixture was then poured into a separatory funnel, and extracted with dichloromethane (3 extractions of 10 mL). The organics were combined and washed with water, followed by a wash with brine before being dried of sodium sulfate. The product was filtered and the solvent evaporated under reduced pressure to yield (acyl)-C7BTBT. Chemical purity was determined by NMR spectroscopy (Figure S8).

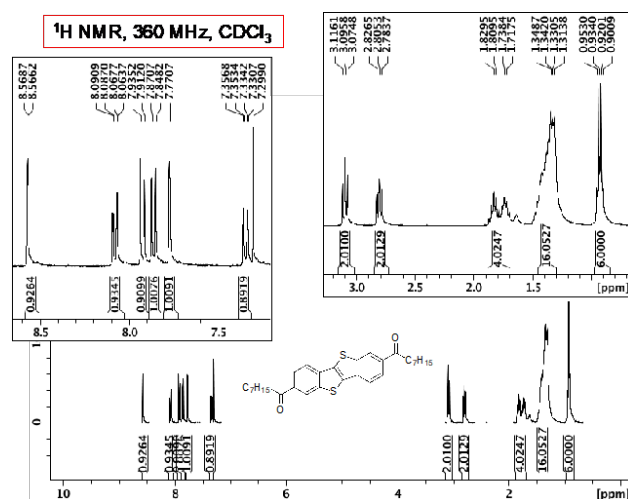


Figure S8: ¹H NMR (CDCl₃) δ: 8.56 (1H, s), 8.06 (1H, d, J = 8.4 Hz), 7.91 (1H, d, J = 8.3 Hz), 7.84 (1H, d, J = 8.1 Hz), 7.77 (1H, s), 7.33 (1H, d, J = 8.2 Hz), 3.09 (2H, t, J = 7.6 Hz), 2.80 (2H, t, J = 7.8 Hz), 1.67–1.88 (4H, m), 1.23–1.50 (16H, m), 0.88–0.96 (6H, m).

1.1.5 c8-BTBT Synthesis

Potassium hydroxide (0.85 g, 15.07 mmol, 5.5 equiv.), (acyl)C7BTBT (1.35 g, 2.74 mmol, 1.0 equiv.), diethylene glycol (140 mL, 0.02 M), and hydrazine monohydrate (64–65% N₂H₄, 4.35 mL, 69.9 mmol,

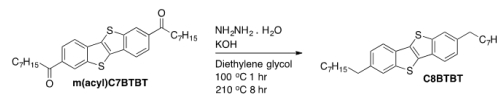


Figure S9: Reaction for c8-BTBT synthesis.

25.5 equiv.) was added to a flame dried flask. The flask was heated in an oil bath at 100 °C for 1 hour, before increasing the temperature to 210 °C for an additional 8 hours. The product mixture was then cooled to room temperature, and poured into water (200 mL) to precipitate the crude product. The precipitate was collected by filtration, and washed with methanol and water. The crude solid product was dissolved in a minimum volume of 1:1 solution of dichloromethane/toluene, then loaded onto silica, and eluted with hexanes. The product solution was evaporated under reduced pressure to yield c8-BTBT. Chemical purity was determined by NMR spectroscopy (Figure S10).

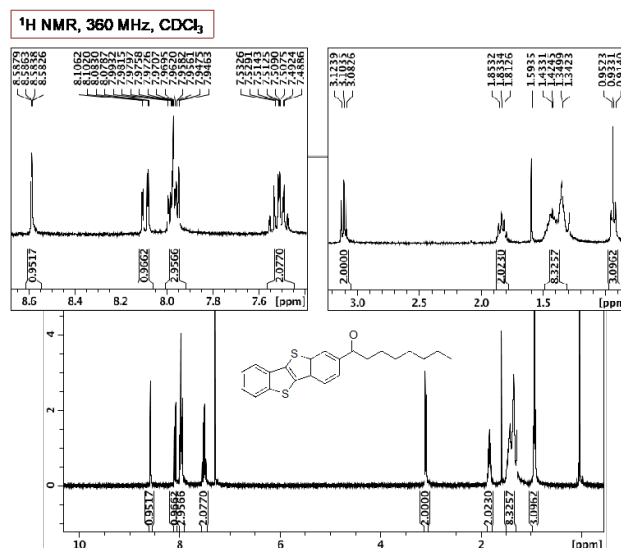


Figure S10: ¹H NMR (CDCl₃) δ: 7.74 (1H, d, J = 8.1 Hz)*, 7.70 (1H, s), 7.15–7.31 (4H, t, m), 2.75 (4H, t, J = 7.9 Hz), 1.65–1.75 (4H, m), 1.22–1.43 (16H, m), 0.91 (6H, t, J = 6.8 Hz).

1.2 Crystal Structures

The six materials studied in this work are [1]benzothieno[3,2-b][1]benzothiophene (BTBT), 2-octyl [1] benzothieno [3,2-b] [1] benzothiophene (m8-BTBT), 2-7-dioctyl [1] benzothien [3,2-b][1] benzothiophene (c8-BTBT), 6,13-bis (triisopropylsilylethynyl) pentacene (TIPS-PN), 5,11-bis (triethylsilylethynyl) anthradithiophene (TES-ADT), and 5,11-bis (triisopropylsilylethynyl) anthradithiophene (TIPS-ADT). The chemical structures for BTBT, m8-BTBT, and c8-BTBT all share a common conjugated core, but differ in the number of side chains attached along the longitudinal axis of the conjugated core. The chemical structures for TIPS-PN, TES-ADT, and TIPS-ADT differ in conjugated core molecules, and side chain structure; the terminal benzene rings in the pentacene are converted into thiophene rings for the ADT molecules, and the TES side chain is smaller than the TIPS side chain in terms of excluded volume.

The crystal structures for the six materials studied are shown in Figure 1. The crystal structures were obtained from refs [3, 4, 5, 6, 7]. For BTBT, m8-BTBT, and c8-BTBT, the herringbone pattern is preserved in the high-mobility plane (Figure 1b, e, and h) indicating that the transfer integrals for the three materials should be comparable. However, we see in Table 1 in the main text that the transfer integral (J_{ij}) for BTBT between the B/C pairs of molecules is significantly reduced compared to the same J_{ij} in c8-BTBT/m8-BTBT. The reason for this reduction comes from the change in the β angle in the unit cell (see Figure 1a, d, and g). This change in angle slightly changes the stacking between molecules, which is enough to reduce $J_{B/C}$ to 1 cm^{-1} from $\sim 600 \text{ cm}^{-1}$ demonstrating how sensitive J_{ij} is to small changes in structure. However, the transfer integrals for m8-BTBT and c8-BTBT are very similar between all pairs, which provides a nice test case to deconvolute the effects of phonons on J_{ij} .

The substituted acenes (TIPS-PN, TES-ADT, and TIPS-ADT) have much more variance in crystal structure than the substituted BTBT's. TIPS-PN and TES-ADT have the most similar crystal structure, but the β angle of the unit cell dramatically

Table 1: Experimental lattice parameters of all six materials. Lattice parameters relevant to charge transport in the high mobility plane are in bold.

Material	a (Å)	b (Å)	c (Å)	α (deg)	β (deg)	γ (deg)
BTBT	11.887	5.889	8.118	90	106.536	90
m8-BTBT	5.942	7.863	40.516	87.972	86.677	89.787
c8-BTBT	5.927	7.88	29.18	90	92.44	90
TIPS-PN	7.565	7.750	16.835	89.15	78.42	83.63
TES-ADT	6.732	7.251	16.695	98.14	94.53	103.92
TIPS-ADT	8.787	17.697	12.107	90	90.46	90

Table 2: Computed lattice parameters of all six materials. Lattice parameters relevant to charge transport in the high mobility plane are in bold.

Material	a (Å)	b (Å)	c (Å)	α (deg)	β (deg)	γ (deg)
BTBT	11.87	5.981	7.914	90	106.1	90
m8-BTBT	6.085	7.489	40.34	88.85	87.50	89.86
c8-BTBT	6.050	7.371	28.86	90	93.39	90
TIPS-PN	7.458	7.727	16.50	90.38	80.67	84.76
TES-ADT	6.614	7.227	16.74	98.28	94.94	102.7
TIPS-ADT	8.766	17.86	12.02	90	89.80	90

changes (Figure 1l, o), which offsets the conjugated cores in TES-ADT such that the cores are not overlapping when viewing the unit cell along the b axis. The offset in conjugated cores significantly changes the frontier orbital hybridization, changing the observed transfer integrals between TIPS-PN and TES-ADT (Table 1). For TES-ADT, the offset changes the values of the transfer integrals in a way that is very beneficial for charge transport [8]. Thus, small chemical modifications can be used to improve charge transport by engineering better transfer integrals. TIPS-ADT shares more chemical similarities to TIPS-PN than does TES-ADT, but the crystal structure of TIPS-ADT completely changes from a brickwork pattern in the high mobility plane (seen in TIPS-PN, Figure 1j, k) to a 1-D slip-stack pattern (TIPS-ADT, Figure 1p, q). The change in crystal structure for TIPS-ADT switches the typical 2-D charge transport to 1-D transport, which is enough to explain the observed reduction in μ_H [9, 10].

Table 2 shows the lattice parameters for all six materials computed with DFT using the optPBE-vdW functional. To demonstrate which functional best represents the experimental XRD structures from lit-

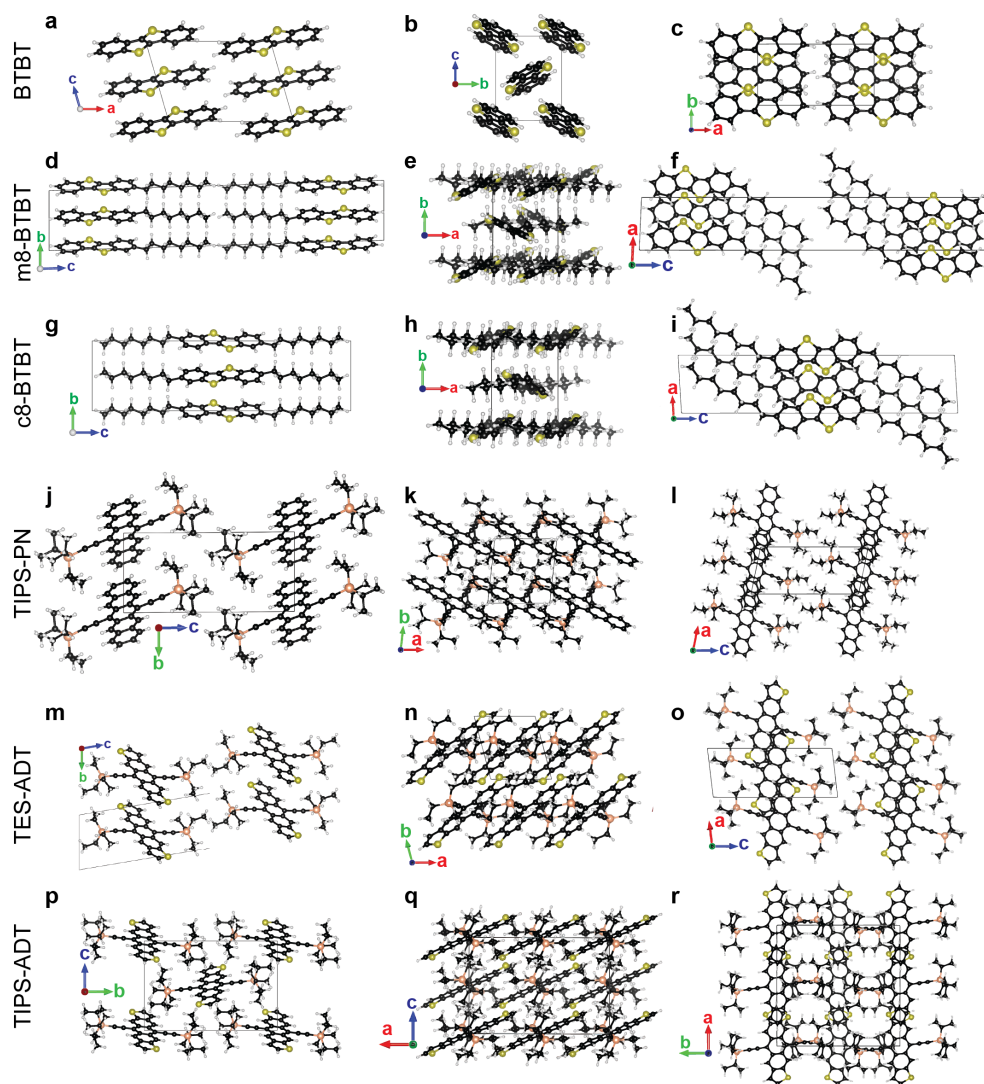


Figure S11: Unit cell structures of BTBT (a, b, c), m8-BTBT (d, e, f), c8-BTBT (g, h, i), TIPS-PN (j, k, l), TES-ADT (m, n, o), and TIPS-ADT (p, q, r) projected along the three crystallographic axes.

Table 3: Computed lattice parameters for BTBT for all functionals tested.

Functional	a (Å)	b (Å)	c (Å)	α (deg)	β (deg)	γ (deg)	Error (Å)
PBE-D3+BJ	11.770	5.886	7.783	90	105.93	90	0.1183
PBE-TS	11.745	5.903	7.813	90	105.59	90	0.1122
revPBE-vdW	11.981	6.137	8.062	90	106.29	90	0.0904
optPBE-vdW	11.857	5.981	7.914	90	106.07	90	0.0753
optB88-vdW	11.748	5.889	7.708	90	105.87	90	0.1443
optB86b-vdW	11.772	5.885	7.675	90	105.66	90	0.1526
rPW86-vdW	11.853	6.032	7.973	90	106.80	90	0.0688

erature, we compare computed lattice parameters and XRD lattice parameters for BTBT in Table 3. The error in Table 3 is computed as,

$$Error = \sqrt{\sum_{lattice} \frac{(l_{XRD} - l_{DFT})^2}{3}} \quad (1)$$

where the sum runs over all lattice parameters (a, b, c) but not any angles. Thus, the error has units of Å, which makes it comparable with the lattice parameters themselves.

1.3 XRD of c8-BTBT

In the main manuscript, we show a low temperature polymorphism of c8-BTBT that results in an inconsistency between the DFT simulation result and the measured INS spectrum. We perform room temperature X-Ray diffraction (XRD) on our c8-BTBT single crystal sample, and compare against the crystal structure from literature [3] (Figure S12a). We demonstrate near perfect agreement between our XRD results and the crystal structure from literature, which we use as an initial structure for our DFT simulations presented in the main text.

After geometry optimization, the simulated crystal structure of c8-BTBT can deviate from the published structure. Figure S12b compares the XRD data of our single crystals to the equilibrated simulated structure. The comparison shows reasonable agreement except for peak at 23°, and the peak at 27.5°, where the simulated reflections are shifted to higher angles indicating that the simulated unit cell is compressed. This compression is expected because the DFT simulation effectively assumes a tempera-

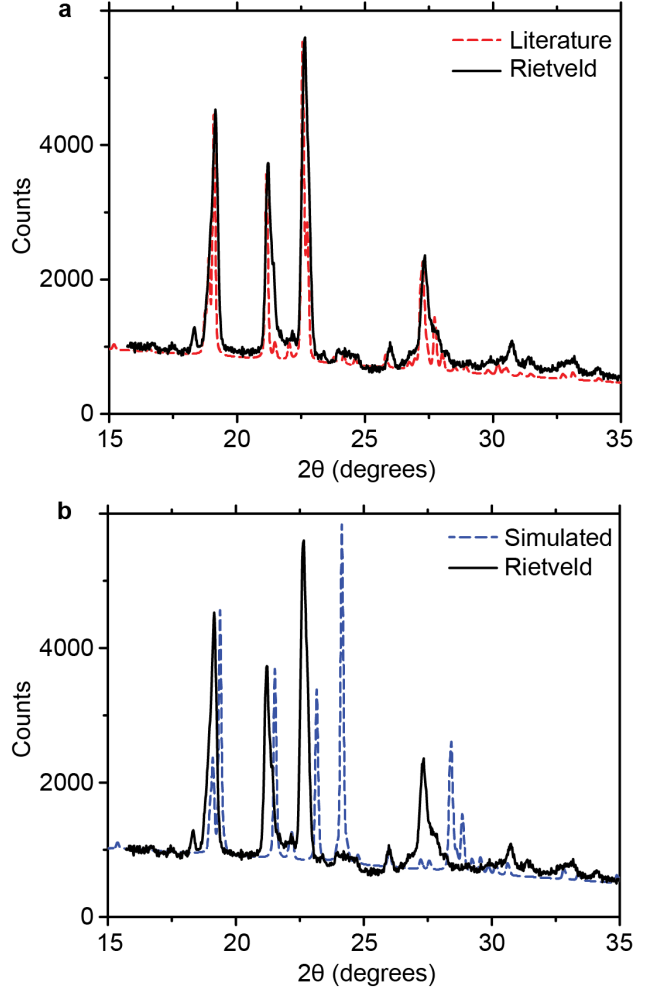


Figure S12: (a) X-Ray diffraction pattern of c8-BTBT (black line) compared against the publicly available crystal structure (red dotted line). (b) X-Ray diffraction pattern of c8-BTBT (black line) compared against the DFT optimized structure (blue dotted line).

ture of 0 K, as the minimization algorithm seeks the lowest energy structure. We expect a certain amount of thermal expansion from the 0 K simulated structure, which would create better agreement between simulation and experiment. Overall, the experimen-

tal XRD pattern in Figure S12a supports our use of the previously reported crystal structure for c8-BTBT since no massive structural reorganization occurs. Thus, the poor agreement between the INS data and simulated spectrum strongly suggests that c8-BTBT recrystallizes into a different structure as the sample is cooled to 5 K for the neutron measurement. Since we are interested in the room temperature hole mobility of c8-BTBT, we use the simulated phonons (Figure 2 of the main text) for the electron-phonon coupling parameters (and later hole mobility calculations) because the simulated c8-BTBT phonons more closely correspond to the room temperature structure.

2 Inelastic Neutron Scattering

Inelastic neutron scattering (INS) is a technique for measuring the vibrational dynamics of a material. The INS spectrum is interpreted within the harmonic approximation for the nuclear motions, assuming that all oscillators are in the ground state, since the measurement is carried out at 5 K. In the case of ground state oscillators, the neutron transfers energy to the material, which is measured in terms of time-of-flight as the reduced energy neutron takes longer to reach the detector than a neutron that did not transfer energy to the material. The probability that a neutron is scattered with a particular energy depends on the orientation of the oscillators, the overall momentum transfer of the process, and the nuclear cross-section of the scattering atom. The combination of all these factors is described by the scattering law in Equation 2,

$$S(\vec{q}, \omega) = \sum_{l, \nu} \sum_{n=0}^{n \rightarrow \infty} \sigma_l \frac{(\vec{q} \cdot \vec{u}_{l, \nu})^{2n}}{n!} e^{-\frac{1}{3} \sum_{\nu} (\vec{q} \cdot \vec{u}_{l, \nu})} \delta(\omega - n\omega_{\nu}) \quad (2)$$

where $\vec{u}_{l, \nu}$ is the displacement of atom l that occurs as a result of phonon mode ν , \vec{q} is the momentum transfer vector of the scattered neutron, σ_l is the neutron scattering cross section of atom l , n is the excitation level of the oscillator resulting from the scattering event (0 is the ground state, 1 is the first excited state, etc.), and $\omega_{l\nu}$ is the frequency of mode

ν . Equation 2 has a vector dependence of \vec{q} , which comes from the alignment of the crystal structure relative to the direction of the incident neutron beam. In order to avoid selectively silencing specific modes and improve signal to noise, we measure the entire powder of randomly oriented crystals, which removes the directional dependence of \vec{q} from our subsequent analysis. Inspection of equation (2) reveals that reconstruction of a scattering function from molecular simulation requires only the set of phonon modes (vibrational modes in isolated molecules) and their associated mode frequencies.

The VISION spectrometer is an inverted geometry instrument, which means that a “white” beam of neutrons (i.e. neutrons over a wide energy range) scatters off the sample, and analyzer crystals positioned at scattering angles of $\sim 45^\circ$ and $\sim 135^\circ$ reflect neutrons with a particular energy to the detectors. The full details of the instrument can be found in refs [11, 12]. The VISION spectrometer is particularly well suited for vibrational analysis due to the high flux and high signal-to-noise, providing excellent vibrational information down to the linewidth of the elastic peak. The setup of the instrument generates spectra with error bars typically smaller than the 1 point linewidth on all Figures in the main text. Since the analyzer crystals are positioned at high and low scattering angles, the resulting spectra are the average of high and low momentum transfer scattering events. As a result, the spectra are not reported with any q dependence; the spectra can be considered averaged over all q points, which means the resulting scattering function only has one variable, the energy transferred.

Figure S13 shows the INS spectra of each material studied over the full energy range. Each peak is the result of a delta function term in Equation 2, broadened by experimental resolution. The width of each curve is scaled by the error bars at each energy transfer; the curves tend to get broader at increased energies ($\sim 3000 \text{ cm}^{-1}$). In addition to the experimental resolution, peaks at low energy are distorted as a result of phonon dispersion, in which the mode energies are affected by the wavelength of the phonon.

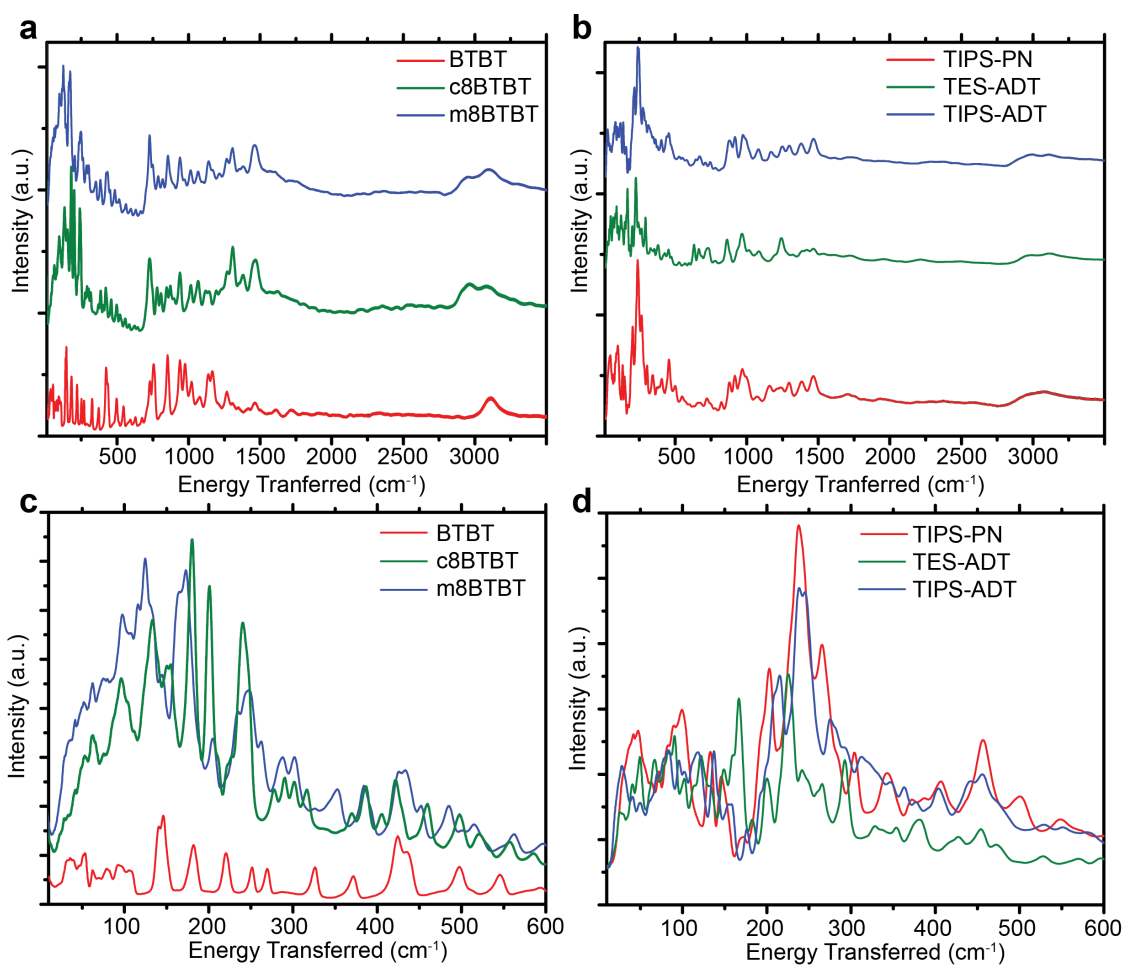


Figure S13: (a,b) INS spectra of BTBT, m8-BTBT, c8-BTBT, TIPS-PN, TES-ADT, and TIPS-ADT over the full energy range relevant for these materials. (c,d) The same spectra plotted from 10 cm^{-1} –600 cm^{-1} to better view the low energy peaks.

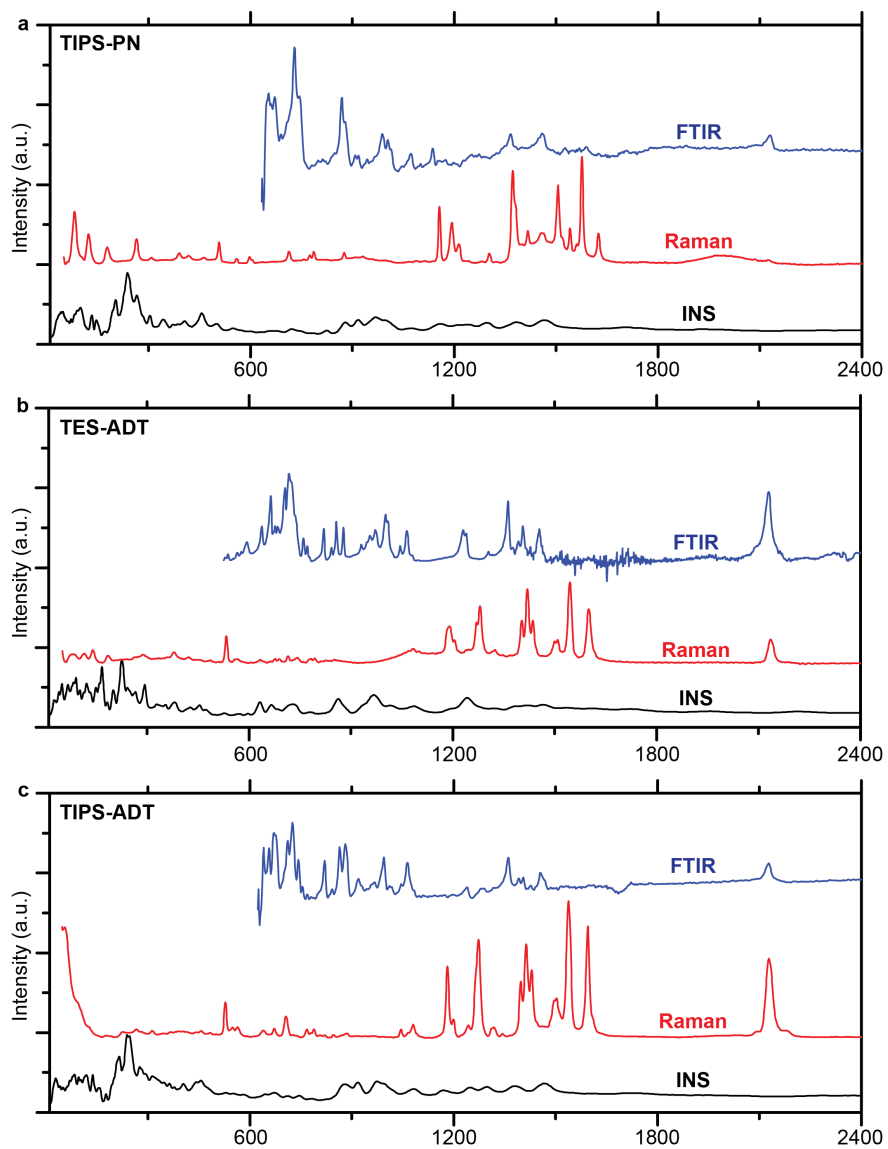


Figure S14: Comparison between INS, Raman, and FTIR for TIPS-PN (a), TES-ADT (b), and TIPS-ADT (c).

3 FTIR and Raman

We use FTIR and Raman spectroscopy to probe motions that are complementary to the motions observed in INS (Figure S14). Between these three measurement techniques, we have measured every possible motion present in the substituted acene materials. The different spectra for each material show peaks in at different energies showing that distinct motions are probed for each measurement. FTIR provides excellent information at high energies with small linewidths and many distinct peaks. However, the measurement is limited to energies $> 600 \text{ cm}^{-1}$, preventing the technique from measuring phonons relevant to charge transport. As an energy loss technique, Raman can probe phonons with energy 200 cm^{-1} ($k_B T$ at 300 K), but the selection rules significantly limit the number of observable peaks below 200 cm^{-1} compared to INS (which has no selection rules). In addition the Raman selection rules limit the observable modes to the gamma point only, limiting the usefulness of Raman when studying charge transport because the phonons at the Brillouin zone boundaries participate most in charge transport. INS provides the most low-energy information for all samples, but INS has the worst resolution at high energy amongst all the techniques. As a result, the three measurement techniques together are ideal for comparing to theoretical simulations to identify the phonons responsible for charge transport.

4 Phonon DFT Simulations

Density functional theory has a large variety of options available to tailor the simulation to any particular situation. In the case of phonon simulations of molecular semiconductors, the choice of dispersion correction is most important because the dispersion forces have a strong impact on low energy phonon modes. In Figure S15, we screen 8 different functionals by comparing the simulated INS spectra to the experimental measurement of BTBT. We seek a few functionals that produce the most accurate gamma point simulations of phonon modes for BTBT, which we will use in more expensive, full

Brillouin zone phonon simulations later. The functionals chosen in Figure S15a/b represent a broad set of different functionals. PBE-D3BJ is the PBE functional [13] with the Grimme dispersion correction with Becke-Johnson damping term [14, 15, 16], PBE-TS is the same PBE functional but with Tkachenko-Scheffler dispersion correction [17], revPBE-vdW is the revPBE functional (adapted from the original PBE functional) with van der Waals energy treated directly in the correlation functional [18], and HSE-06 is a hybrid functional created by Heyd, Scuseria, and Erzerhof that contains a term for the exact Hartree-Fock exchange energy with a range separation parameter that means the linear combination of functionals changes with distance (r) [19]. In principle, HSE-06 is the most accurate, followed by revPBE-vdW, and the pure PBE functionals with dispersion corrections, respectively. However, in practice, the HSE-06 functional needs to be preconditioned with a shorter PBE simulation first, and the simulation still takes too much time after preconditioning, likely due to the computational expense of the exact exchange kernel. Thus, despite the expected accuracy of the HSE-06 functional, we could not continue to use it for further simulations (or any other hybrid functional using exact exchange).

Each simulation was performed at the unit cell length scale, and only the gamma point of the Brillouin zone was used for the calculation to speed up the screening process. As a result, the agreement between simulation and experiment breaks down at low energy. However, since the dispersion of phonon modes decreases with increasing energy, we expect that the peaks at energies $> 200 \text{ cm}^{-1}$ can be used to test the quality of the functional for phonon simulations. In Figure S15a/b, the revPBE-vdW simulation shows reasonable agreement. In addition, this type of functional treats van der Waals interactions more generally, which leads to more consistent results across multiple materials. As a result, we expand the focus on van der Waals density functionals (vdW-DF's) by performing phonon simulations of different vdW-DF's in Figure S15c/d (revPBE-vdW, optB86b-vdW, optB88-vdW, optPBE-vdW, rPW86-vdW) [20, 21, 18, 22, 23, 24], where we identify revPBE-vdW, optPBE-vdW, and optB88-vdW for

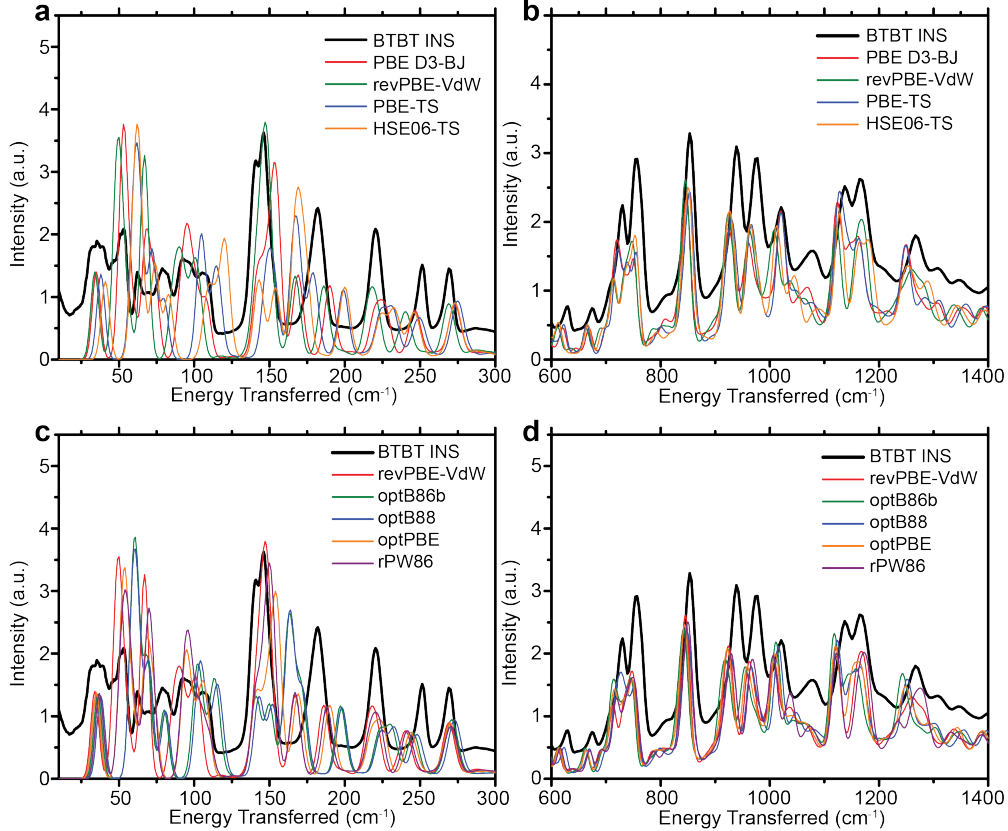


Figure S15: Comparison of INS measurement and DFT simulation while varying the functional. (a,b) The functionals are chosen from a broad class including pure functionals, hybrid functionals, and van der Waals functionals. (c,d) The entire set of van der Waals functionals in VASP 5.4.1 is compared to INS measurement.

further study. The simulated spectra for these three functional demonstrate systematic energetic shifts in the observed peaks (phonon energies): revPBE-vdW peaks are shifted to the lowest energies, optB86b-vdW peaks are shifted to the highest energies, and optPBE-vdW peaks represent a good compromise between the other two functionals.

In Figure S16 we show how simulation design choices such as basis set size, convergence criteria, and electronic k-point sampling density affect phonon simulations. Figure S16a,c demonstrates that the simulation converges with a 520 eV basis set size,

and an electronic k-point Monkhorst-Pack sampling grid of $2 \times 3 \times 2$. In Figure S16b, we show that the electronic convergence tolerance of 10^{-8} eV, and an interatomic force convergence tolerance of $2 \cdot 10^{-3}$ eV/Å is sufficient to converge the simulation (denoted as revPBE_08_002).

To obtain the phonon Brillouin zone sampling density dependence on simulated spectra, we perform $2 \times 2 \times 1$ supercell calculations on c8-BTBT at varying sampling densities (Figure S17a). We observe very little change in simulated spectra at energies above 200 cm^{-1} . Below 200 cm^{-1} , there are some differ-

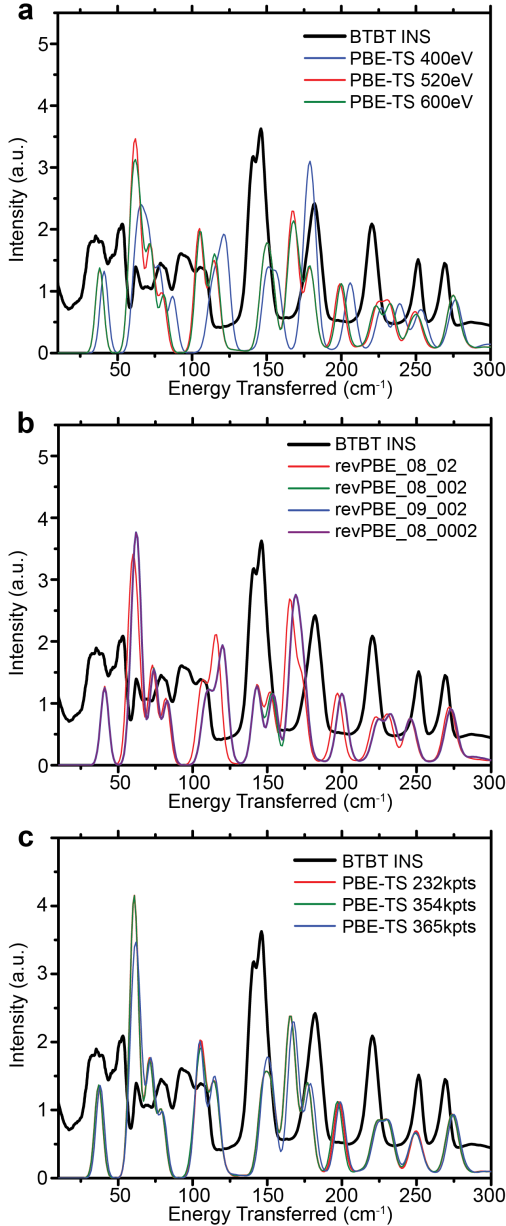


Figure S16: (a,b) INS spectra of BTBT, *m8*-BTBT, *c8*-BTBT, TIPS-PN, TES-ADT, and TIPS-ADT over the full energy range relevant for these materials. (c,d) The same spectra plotted from 10 cm^{-1} – 600 cm^{-1} to better view the low energy peaks.

ences as the higher sampling density simulations have a more rounded structure at low energy. The $4\times 4\times 1$, and $4\times 4\times 2$ sampling grid simulations are effectively the same, demonstrating convergence. In general for any material in the main text, we pushed the sampling density to the maximum file size that could be processed by oCLIMAX (must be run on PC, limiting the available RAM), which we assumed to be effectively converged.

In Figure S17b, we perform phonon simulations on a $2\times 2\times 1$ supercell of BTBT, with a $5\times 5\times 5$ (MP grid) sampling of the phonon Brillouin zone for the three candidate functionals (optB88, optPBE, revPBE). The full Brillouin zone phonon simulation was performed using Phonopy [25], which evaluates the interatomic force constants using finite difference. Simulation of different q -points in the Brillouin zone using the finite difference method requires the assumption that each periodic copy of the perturbed cell does not interact with any other copy. If the lattice parameters of the chosen supercell are too small, a displaced atom in the original cell will impact the forces acting on the displaced atom in an adjacent periodic copy, which will introduce errors in the phonon calculations. Therefore, we used a $2\times 2\times 1$ supercell of BTBT because each lattice dimension was greater than 1 nm. We assumed a supercell of this size should be large enough to minimize errors in the phonon calculations while also minimizing the computational expense of the calculation. Ideally, it would be best to increase the size of the supercell such that each lattice dimension is greater than 2 nm, creating a minimum 1 nm separation between any atom in the supercell and a displaced atom, which is greater than many long-range cutoffs used in molecular dynamics studies [26]. However, such a requirement would increase the computational expense of each simulation by ~ 4 fold. We limit the screening to the three functionals on BTBT only, because each full simulation requires $\sim 300,000$ computer hours at a national supercomputing facility. Additional screening of more complex materials would be unfeasible.

The optPBE functional (green line in Figure S17) almost perfectly mirrors the onset of the low energy peaks around $\sim 100\text{ cm}^{-1}$ (highlighted by the pink region in Figure S17b). The revPBE functional pre-

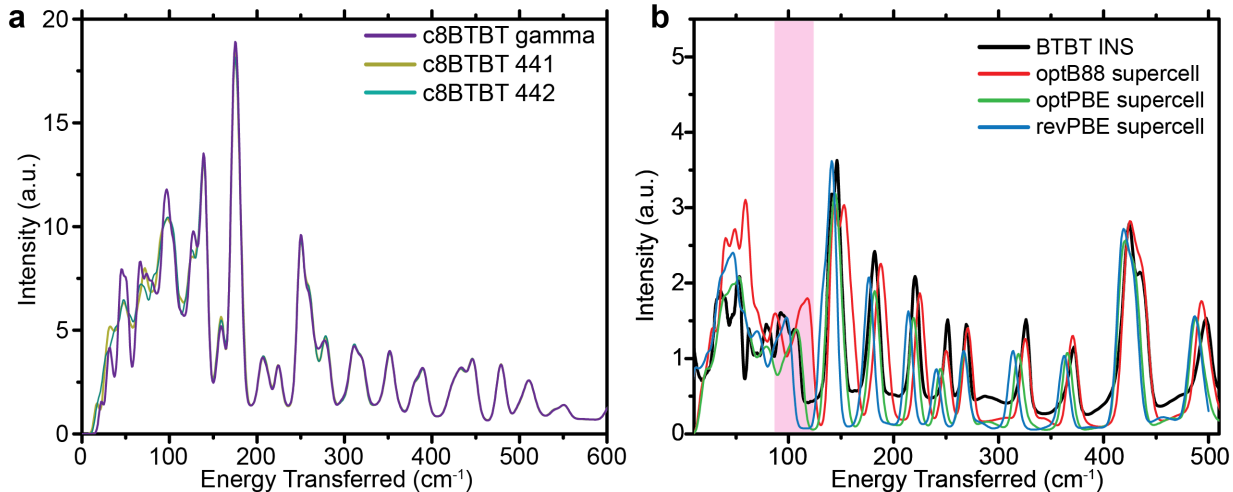


Figure S17: (a) Supercell simulations of c8-BTBT for three different MP sampling grids of the phonon Brillouin zone: gamma point of supercell (purple line), $4 \times 4 \times 1$ MP grid (yellow line), $4 \times 4 \times 2$ MP grid (cyan line). (b) Supercell calculations of BTBT for three different functionals presented in the legend compared against the experimental INS spectrum for BTBT. The pink shaded region emphasizes the portion of the spectrum that clearly differentiates the quality of the simulations produced by the different functionals.

dicts an onset that is too red-shifted, and the optB88 functional predicts an onset that is too blue-shifted. Interestingly, the simulation using the optB88 functional demonstrates better agreement for peaks ≥ 240 cm⁻¹, but, since the description of low energy modes is more important for electron-phonon coupling, we use the optPBE functional for the remainder of the analysis (shown in the main text) for all other materials.

The result of using the optPBE-vdW functional for supercell simulations for other materials over the entire energy is shown in Figure S18. Each simulated spectrum was scaled by 1.015 to better agree with the experimental spectra at high energies. We see excellent agreement between simulated and experimental spectra over an energy range that spans three orders of magnitude, demonstrating that we have reliable information on atomic dynamics on the time scales ranging from 10 fs — 1 ps.

The phonon band structures for all six materials is shown in Figure S19. The symmetry points chosen depends on the symmetry of the respective unit cells;

m8-BTBT, TIPS-PN, and TES-ADT have P-1 symmetry, while BTBT, c8-BTBT, and TIPS-ADT have P₂/c symmetry. The low energy bands show relatively high dispersion (~ 50 cm⁻¹), and the degree of dispersion decreases as the average energy of the band increases. The difference between the minimum and maximum energy in a particular band, called the bandwidth, is a measure of the effective spring constant between molecules in adjacent unit cells. c8-BTBT has the highest amount of dispersion at low energy, which is a reason why c8-BTBT has a low dynamic disorder.

Numerical instabilities lead to negative frequencies in the band structures. The cause for the instabilities is likely due to the size of the super cell, but could also be due to the pronounced anharmonicity of low energy modes or numerical instabilities in the computation of the force constants. In Figure S20, we demonstrate that the average force constant between a pair of atoms decreases exponentially with the distance between the pair of atoms. The average force

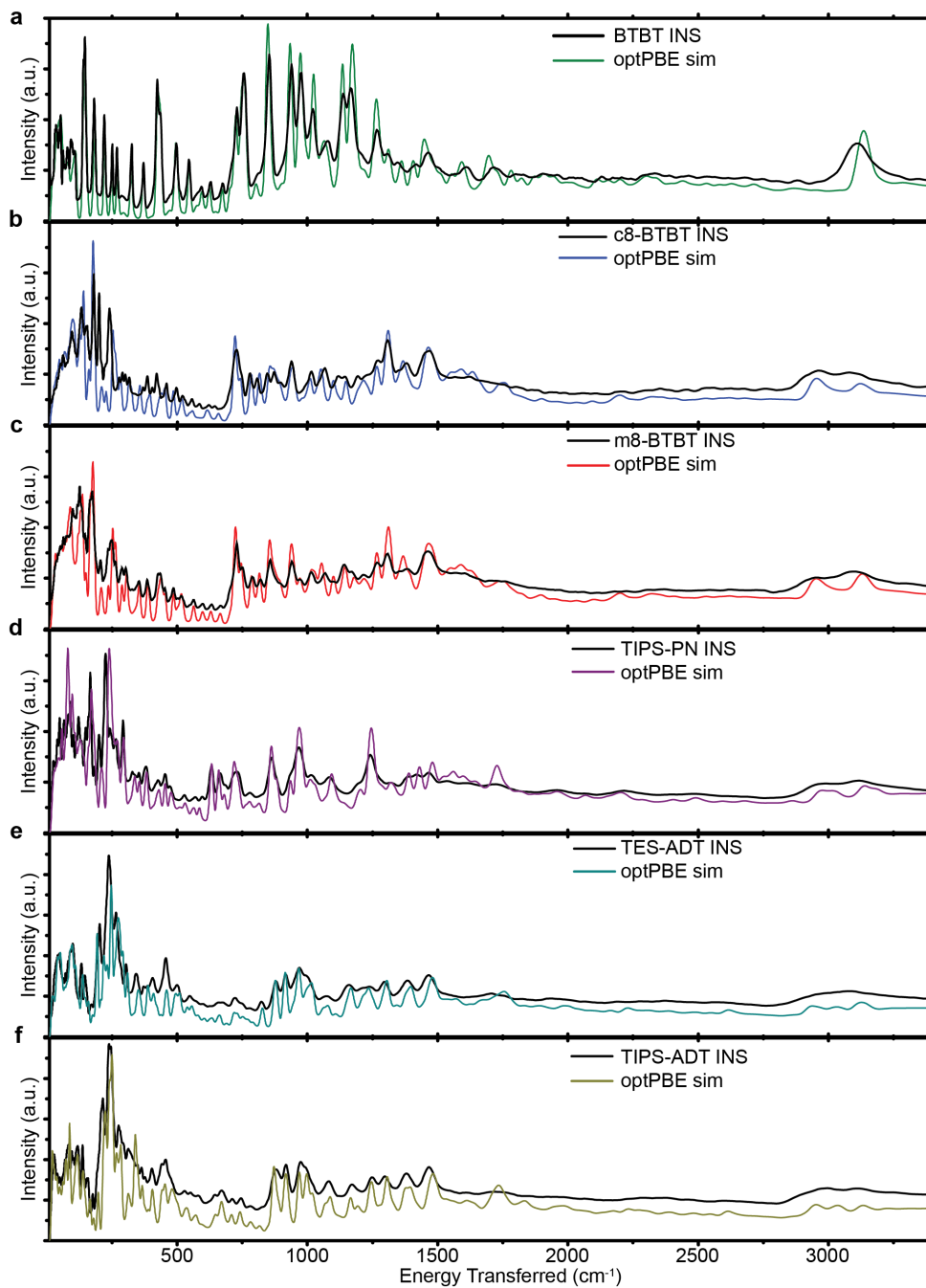


Figure S18: Comparison between experimental INS spectra and optPBE DFT simulations for all six materials studied over the full energy range ($10\text{--}3400\text{ cm}^{-1}$).

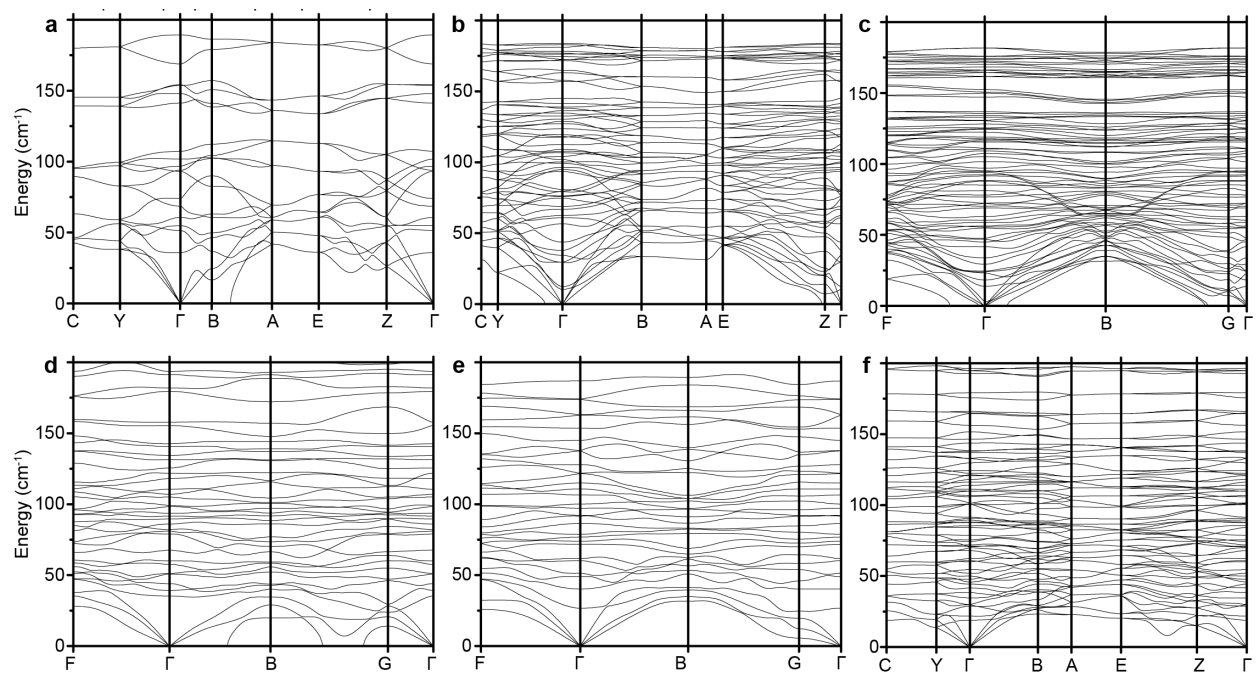


Figure S19: Phonon band structures for BTBT (a), c8-BTBT (b), m8-BTBT (c), TIPS-PN (d), TES-ADT (e), and TIPS-ADT (f).

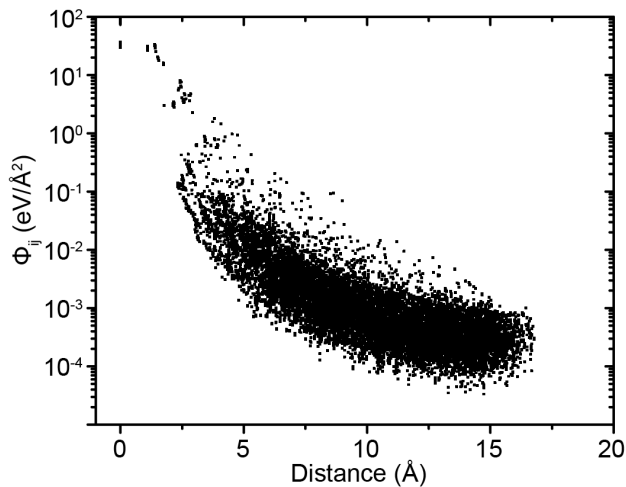


Figure S20: Average force constant between two atoms (i and j) as a function of distance between the pair of atoms.

constant, Φ_{ij} is computed according to:

$$\Phi_{ij} = \sqrt{\sum_{\alpha=1}^3 \sum_{\beta=1}^3 \Phi_{i\alpha,j\beta}^2} \quad (3)$$

where α and β are the Cartesian indices of atoms i and j , respectively. The values for Φ_{ij} exponentially decrease by ~ 6 orders of magnitude over distances in the supercell, which suggests that numerical errors may be the cause of the instability. To test if the negative frequencies are due to numerical errors in the computation of the force constants, we applied a 10 Å cutoff to the force constants for c8-BTBT. The resulting negative branch of the band structure (not shown) became more negative than the branch shown in Figure S19, indicating that numerical errors are likely not the cause of the instability. Instead, the likely reason for the instability is because we limited the size of the supercell in the side chain direction to be equal to that of the primitive cell (e.g. supercell for c8-BTBT is 2x2x1, where the “1” is in the side chain direction). The weak van der Waals interactions, which are dominant between adjacent high mobility planes, do not decay quickly with distance,

meaning the periodic image interacts with the original supercell causing the small instability. The reason we truncated the supercell in the side chain direction was to decrease the computational load; a 2x2x1 supercell of m8-BTBT has 768 atoms, and we would need at least a 2x2x2 supercell for each BTBT-based material. As a result, our simulations can not accurately compute the energies of the phonon branch in which the phonon polarization and wavevector are collinear along the side chain axis direction.

No phonons with negative frequencies were included in our models for dynamic disorder in the main text. Many of the materials show acoustic phonon instabilities near the Γ point, but those low energy modes have very low associated EP coupling parameters due to their high wavelengths (see Figure 4 in the main text). The instabilities near the Brillouin zone boundaries (Figure S19b,c) are not relevant to charge transport because those modes are acoustic modes with a primary oscillation direction parallel to the long axis of the unit cell (side chain direction), and the wavevector (q -position in Brillouin zone) of the unstable branch is perpendicular to the high mobility plane, which means the molecules are not displaced relative to other molecules in the same high mobility plane, and thus have nonlocal EP coupling values that are exactly zero. Thus, it is not important to accurately simulate this phonon branch when computing μ_h . Additionally, the single unstable branch does not significantly decrease the accuracy of the simulated INS spectra in Figure S18.

The simulated phonons were also used to compare to the FTIR spectra for TIPS-PN, TES-ADT, and TIPS-ADT in Figure S21. To accurately determine which modes are IR active in the solid state, we computed the Born effective charge tensors for each atom in the unit cell. The agreement between simulations and experimental spectra is good; the simulated spectra were not scaled at all (unlike the INS simulations). This means that the FTIR peaks are shifted relative to the INS spectra, which is likely due to the temperature of the measurement; FTIR was done at room temperature, and INS was done at 5 K.

Since optical modes such as Raman and FTIR spectroscopy only probe gamma point phonons, we compute the dynamic disorder for each material

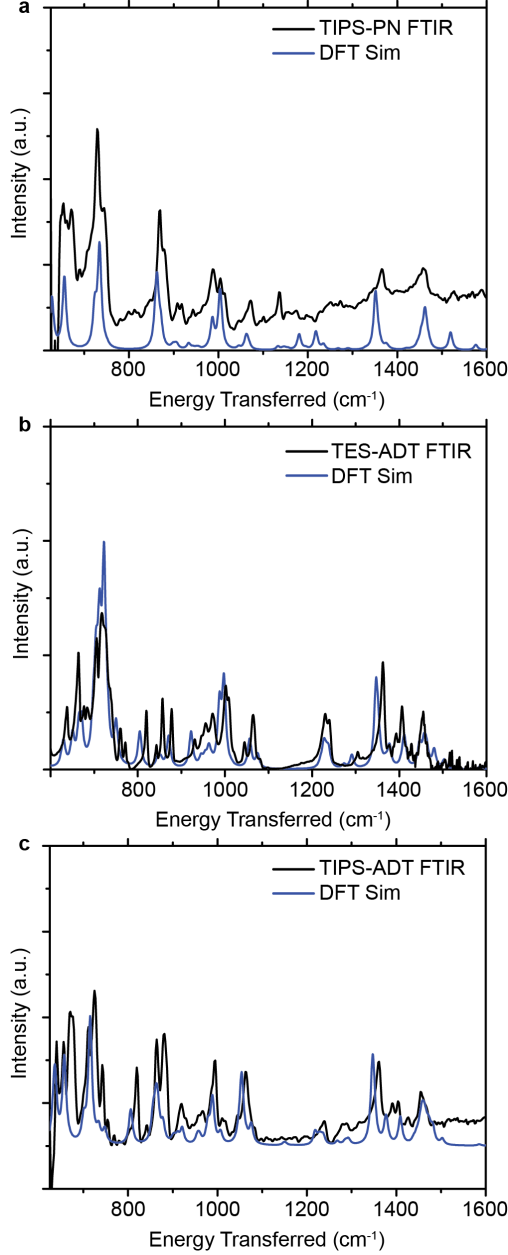


Figure S21: Comparison between FTIR spectra and DFT IR-active phonons for (a) TIPS-PN, (b) TES-ADT, and (c) TIPS-ADT.

Table 4: Computed dynamic disorder including full Brillouin zone phonons (σ), and including only gamma point phonons (σ_{gamma}).

Material	Pair	σ (cm^{-1})	σ_{gamma} (cm^{-1})	Relative Error (%)
c8-BTBT	A	210	233	11.0%
	B/C	367	458	24.8%
BTBT	B/C	39.0	24.4	62.6%
	A	256	247	96.4%
m8-BTBT	A	254	281	10.5%
	B	547	569	4.11%
	C	535	543	1.50%
TIPS-PN	B	311	238	-23.6%
	C	124	121	-2.48%
TES-ADT	C	439	338	-22.9%
	B	223	205	-8.16%
TIPS-ADT	A	279	265	-4.94%

using only the gamma point phonons in Table 4. We demonstrate that there is a -40%—25% relative change between full Brillouin zone dynamic disorder and gamma point dynamic disorder. Thus, methods that only probe gamma-point phonons do not contain enough information to accurately parametrize the nonlocal EP coupling in these materials.

5 Electron-Phonon Coupling

The electronic Hamiltonian for a narrow band material like a molecular semiconductor can be written as

$$H^{el} = \sum_{\{ij\}} J_{ij} |i\rangle \langle j| \quad (4)$$

where the basis set $\{|i\rangle\}$ contains one-electron states localized on site i . Only one state per site is considered (e.g. the molecular HOMO for hole transport), the summation is limited to nearest neighbor pairs (defined in Figure S22), and J_{ij} is the transfer integral. The Hamiltonian representing the non-local electron-phonon coupling contains the modulation of the transfer integral due displacements along a nuclear mode Q_I :

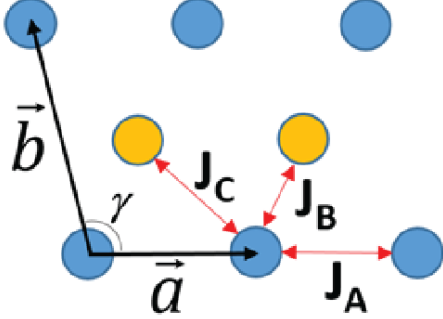


Figure S22: Definition of a standard 2D lattice used to present the parameters needed for the calculation of the mobility. The x direction is parallel to a .

$$H^{el-ph} = \frac{1}{\sqrt{N_q}} \sum_{\{ij\}} \sum_I g_{ij,I} Q_I |i\rangle \langle j| \quad (5)$$

where the $g_{ij,I}$ are the non-local electron-phonon couplings, the index I run on all nuclear modes and N_q is the number of q points that are sampled (as we use calculations in supercells and various q points for each supercell, the index I combines the labels of wave-vector and mode). The nuclear displacements are expressed in dimensionless coordinates and the phonon Hamiltonian can be therefore written as

$$H^{ph} = \sum_I \hbar\omega_I \left(-\frac{1}{2} \frac{\partial^2}{\partial Q_I^2} + \frac{1}{2} Q_I^2 \right) \quad (6)$$

where $\hbar\omega_I$ are the phonon energies.

To make a connection between the generic Hamiltonian and the computational results we note that the transfer integrals can be computed at different geometries and indicated with $J_{ij}(\{Q_I\})$. The transfer integral at null displacement is the one entering into equation (4), i.e. $J_{ij}(\{Q_I\} = 0) = J_{ij}$. The electron phonon couplings are the derivative of the transfer integral computed at the equilibrium position i.e.

$$g_{ij,I} = \left(\frac{\partial J_{ij}(\{Q_I\})}{\partial Q_I} \right)_{\{Q_I\}=0} \quad (7)$$

In practice the transfer integrals are computed for the interacting molecular pairs as reported in ref. [27] using the B3LYP/6-31G* method and equation (7) is evaluated by numerical differentiation. It is convenient for computational reasons and to provide an intuitive picture of the EP coupling to use Cartesian displacement to evaluate equation (7). Indicating with \vec{Q}_I the Cartesian representation of the dimensionless displacement along mode I and with $\vec{\nabla} J_{ij}$ the gradient of the transfer integral for Cartesian displacements of all atoms (at equilibrium), the EP coupling can be rewritten as:

$$g_{ij,I} = \vec{\nabla} J_{ij} \cdot \vec{Q}_I \quad (8)$$

Equation (8) highlights that the strongest EP couplings are found when the polarization of the normal modes are more parallel to the gradient of the transfer integral.

One can see from equation (5) that each EP coupling term contributes to the variance of J_{ij} through an additive term $|g_{ij,I}|^2 \langle Q_I^2 \rangle$, where the average squared displacement along each mode depends on the thermal energy $k_B T$ and the mode energy. The overall variance can be expressed as in equation (3) of the main manuscript:

$$\sigma_{ij,T}^2 = \frac{1}{N_q} \sum_I \frac{|g_{ij,I}|^2}{2} \coth \left(\frac{\hbar\omega_I}{2k_B T} \right) \quad (9)$$

Since we are also interested in understanding the spectral decomposition of the EP coupling, we define a spectral density according to eq 10. Such a decomposition allows an intuitive comparison between phonon time scales ($1/\omega_I$), and electronic transport time scales (\hbar/J_{ij}).

$$B_{ij}(\omega) = \frac{1}{N_q} \sum_I |g_{ij,I}|^2 \delta(\hbar\omega - \hbar\omega_I) \quad (10)$$

$B_{ij}(\omega)$ is related to $\sigma_{ij,T}$ through equation (11).

$$\sigma_{ij,T}^2 = \int_0^\infty \frac{B(\omega)}{2} \coth \left(\frac{\hbar\omega}{2k_B T} \right) d(\hbar\omega) \quad (11)$$

Equations (11) and (9) are identical because $|g_{ij,I}|^2$ contains the scalar product of $\vec{\nabla} J_{ij}$ and the phonon

eigenvector, and the ground state mean squared displacement of mode I . $B(\omega)$ can be broken down into two components; (1) the average EP parameter ($g_{ij,I}$) at energy $\hbar\omega$, and (2) the density of states at energy $\hbar\omega$. This decomposition of $B(\omega)$ is important to consider in the context of phonon engineering because the phonon density of states can be engineered to have more states at higher energy, and the phonon eigenvectors can be engineered to oscillate in directions that do not vary J_{ij} (i.e. the phonon eigenvector is orthogonal to $\vec{\nabla}J_{ij}$). Both design principles lead to a reduction in overall EP coupling. We define the EP coupling spectrum averaged over the full phonon DOS according to equation (12).

$$|g_{avg}^{full}(\omega)|^2 = \frac{\sum_I |g_{ij,I}|^2 \delta(\hbar\omega - \hbar\omega_I)}{\sum_I \delta(\hbar\omega - \hbar\omega_I)} \quad (12)$$

Equation (12) can be rewritten in a simpler form, considering that the density of states can be written according to equation (13).

$$\rho(\omega) = \frac{1}{N_q} \sum_I \delta(\hbar\omega - \hbar\omega_I) \quad (13)$$

We immediately see that the numerator is proportional to $B(\omega)$. If we make a further simplification that the portion of the phonon density of states that participates in EP coupling is due to motion of the atoms in the conjugated core, then we can use the projected density of states (called PDOS, given in equation (14)) instead of the full density of states.

$$\rho_{proj}(\omega) = \frac{1}{N_q} \sum_I \vec{Q}_I \cdot \overline{\overline{D}} \cdot \vec{Q}_I \delta(\hbar\omega - \hbar\omega_I) \quad (14)$$

The vector \vec{Q}_I is the eigenvector for mode I , and $\overline{\overline{D}}$ is a diagonal matrix projecting the eigenvector onto the conjugated core atoms in the supercell, and N_q is the number of sampled q-points. The advantage of using PDOS over the full DOS is that the full DOS will have many peaks that do not contribute to EP coupling at all, making the PDOS a much more accurate descriptor of the density of states that actually contribute to EP coupling. In addition, we remove the inherent

dependence of $|g_{avg}^{full}(\omega)|^2$ on the number of atoms in the supercell because the full DOS is proportional to the number of atoms, which would make J 's from materials with larger side chain structures seem less responsive to phonons than they truly are. Thus, we define the average spectrum of EP coupling that actually participates in charge transport (i.e. projected onto the conjugated core) in 15.

$$|g_{avg}(\omega)|^2 = \frac{B(\omega)}{\rho_{proj}(\omega)} \quad (15)$$

This average function is distinct from $|g_{avg}^{full}(\omega)|^2$ as the average over the full DOS, which averages over modes that have near zero values of $|g_{ij,I}|^2$ (i.e. side chain twists, bends, and/or stretches), producing unwanted artifacts in the function. With the definition of $|g_{avg}|^2$ in hand, we can write an equation for $\sigma_{ij,T}$ that clearly separates the different contributions, both of which can be engineered independently.

$$\sigma_{ij,T}^2 = \int_0^\infty |g_{avg}(\omega)|^2 \frac{\rho_{proj}(\omega)}{2} \coth\left(\frac{\hbar\omega}{2k_B T}\right) d(\hbar\omega) \quad (16)$$

In equation (16), we note that $|g_{avg}(\omega)|^2$ takes the role of the average scalar product between transfer integral gradient and the conjugated core portion of the eigenvector at a particular energy. Thus, $|g_{avg}(\omega)|^2$ is a material-specific function that determines how likely an average phonon at a given energy interacts with charge transport.

The PDOS is a useful description of the thermal disorder associated with the backbone. In the main manuscript, we discuss the average EP coupling and PDOS of m8-BTBT, and c8-BTBT to rationalize the observed differences in the overall fluctuation of J_{ij} ($\sigma_{ij,T}$). The average EP coupling, and PDOS are repeated in Figure S23 for completeness. Changes in the transfer integral fluctuation, $\sigma_{ij,T}$ (Table 1 in the main text), come from changes in the projected density of states (PDOS, equation (14)) for the backbones, and changes in intrinsic EP coupling values. Modifying the BTBT molecule with side chains has the effect of increasing the phonon energies such that there is a decrease in the PDOS in the low energy

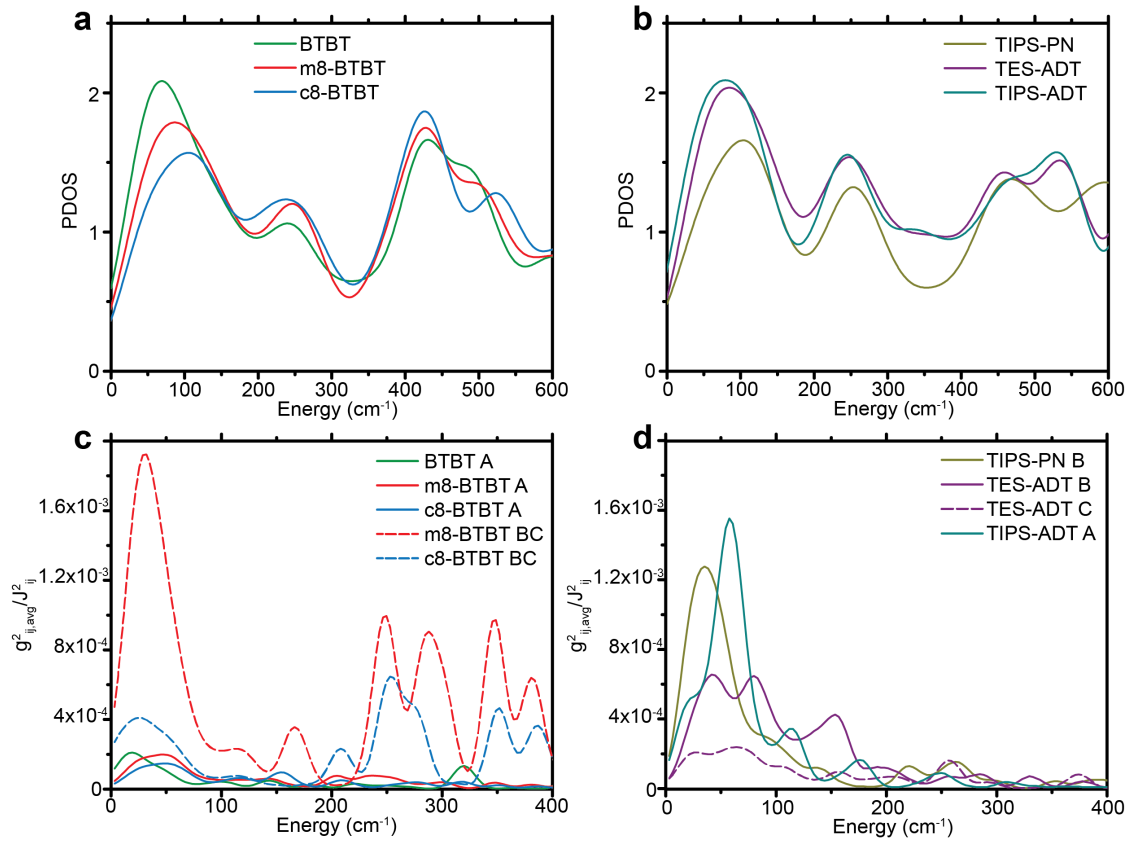


Figure S23: (a,b) Phonon density of states projected onto the backbone atoms, and (c,d) Average electron-phonon coupling spectrum (functional form defined in text) for all six materials .

region of the spectrum (Figure S23). We have normalized the PDOS curves such that the total integral is equal to unity and so each PDOS curve in Figure S23 is comparable. There is a shift in the PDOS to higher energies as the BTBT backbone is modified with more side chains, reinforcing the idea, suggested by Illig et. al [28] and in the main text, that the side chains “lock” the backbone into place increasing μ_h . The shift in the PDOS to higher energies means that mobile charges are less likely to be affected by phonons because the higher energy phonons have lower occupation numbers at room temperature, leading to smaller displacements and less disorder.

Now we consider the effect of $|g_{avg}(\omega)|^2$ on μ_h for BTBT. We show that the average EP coupling in the A transport direction (shown in Figure S23c) is lowest for c8-BTBT, and the average EP coupling for BTBT and m8-BTBT appears to be comparable. The normalized $|g_{avg}(\omega)|^2$ for m8-BTBT is much greater than c8-BTBT in the B/C transport directions. We do not show the normalized $|g_{avg}(\omega)|^2/J^2$ spectrum for BTBT in the B/C directions because the peaks in that spectrum is normalized by a factor ($J_{B/C}$) that is much smaller than the other materials. When comparing the spectra for m8-BTBT and c8-BTBT, the reduction in the $|g_{avg}(\omega)|^2$ at low energy is due to the change in phonon polarization because ∇J_{ij} is identical between m8-BTBT and c8-BTBT. The observed differences between BTBT and c8-BTBT are attributed to changes in the average scalar product between ∇J_{ij} and the phonon polarizations. The subtle differences in unit cell structure for BTBT could change ∇J_{ij} as well as the phonon polarization, which increase the observed $|g_{avg}(\omega)|^2$ at low energy.

To deconvolute the different aspects affecting μ_h in the substituted pentacene group of materials, we compare the two pair with the same crystal structure, TIPS-PN/TES-ADT, and a pair with different crystal structures, TES-ADT/TIPS-ADT.

For the TIPS-PN/TES-ADT pair, the most important structural difference is the offset of the conjugated cores of the TES-ADT crystal structure (most easily seen in Figure 1o). To understand the reduced relative dynamic disorder ($\sigma_{ij,T}/|J_{ij}|$) in TES-ADT

relative to TIPS-PN, we first consider the PDOS distributions. Here we choose to use $\sigma_{ij,T}/|J_{ij}|$, instead of $\sigma_{ij,T}$ (as used in the main text) because $\sigma_{ij,T}/|J_{ij}|$ is more closely correlated to μ_h for materials with significantly different values for J_{ij} [8]. In Figure S23b, there is an increase in the lowest energy peak of the TES-ADT PDOS relative to the same peak in the TIPS-PN PDOS, which contradicts the increase in computed μ_h . Interestingly, the PDOS for TIPS-ADT is very similar to the PDOS of TES-ADT (Figure S23b), indicating that the change in backbone structure (from pentacene to ADT) significantly contributes to unfavorable changes to the PDOS (could be due to softer intermolecular interactions of sulfurs). Instead, the difference in $\sigma_{ij,T}/|J_{ij}|$ is explained by the average EP coupling spectra in Figure S23d. The acoustic modes in TES-ADT are less responsive to charge transport than in TIPS-PN. The fundamental cause of the change in interaction is unknown at this time, as we cannot deconvolute the changes in the transfer integral gradient (∇J_{ij} in the main text) from the change in the direction of atomic oscillations due to phonons.

Since all curves in Figure S23 are normalized, we can directly compare the PDOS for all materials, and average EP coupling spectra between any of the six materials. In the main text, we show that TES-ADT, and c8-BTBT are the two materials with highest μ_h from the two structural families, so we compare them here to assess why c8-BTBT is a better conductor than the TES-ADT. C8-BTBT has a reduced PDOS at low energy, and the peak is shifted to higher energies, and has lower average EP coupling at low energy, but TES-ADT has the higher μ_h using the unmodified version of transient localization theory. To explain this, we point to the work of Fratini et al. in ref [8], in which the authors elucidated the importance of the relative sign and magnitude of the set of transfer integrals. However, a much larger proportion of the EP coupling spectrum for c8-BTBT is above 200 cm^{-1} compared to the EP spectrum of TES-ADT. After accounting for these differences, c8-BTBT has a higher simulated μ_h , which agrees with experimental values.

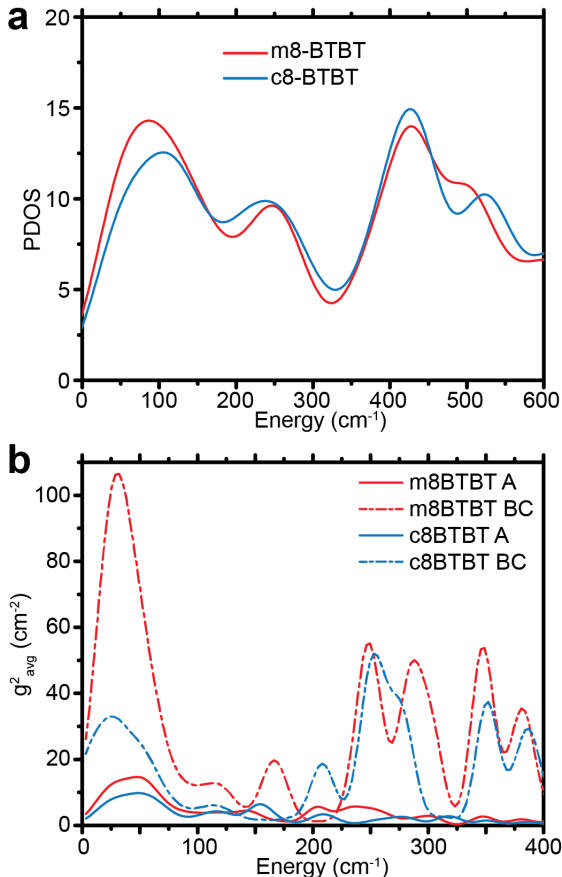


Figure S24: (a) Phonon density of states projected onto the backbone atoms, and (b) average electron-phonon coupling spectrum for distinct transport directions of m8-BTBT and c8-BTBT.

5.1 Comparison Between EP Coupling in c8-BTBT and m8-BTBT

The three primary contributions to $\sigma_{ij,T}$ are the direction of the phonon polarization vector, the direction/magnitude of the gradient of the transfer integral with respect to atomic coordinates ($\vec{\nabla}J_{ij}$), and energy of phonons. The polarization vector is the set of vectors defining the direction of motion for each atom in a particular phonon mode. Any EP coupling parameter can be expressed as the scalar

product between $\vec{\nabla}J_{ij}$ and phonon polarization vector (more details available in SI section 5). Changes in the direction of the phonon polarization vector affects EP coupling because the polarization vector may be more orthogonal to $\vec{\nabla}J_{ij}$, minimizing the impact of the particular mode on charge transport. The energy of a phonon mode ($\hbar\omega_T$) contributes to $\sigma_{ij,T}$ by controlling the strength of the temperature factor in equation (3), which gives much greater weight to phonons with energy below $k_B T$.

To engineer materials with improved μ_h through reduced $\sigma_{ij,T}$, we must correlate changes in structure to changes in the three aforementioned contributions. Since our DFT simulations provide both $\vec{\nabla}J_{ij}$ and complete information of every atomic motion for all phonon modes in the system, we can begin to deconvolute how the underlying contributions of $\sigma_{ij,T}$ are impacted by changes in structure.

As an illustrative example, we focus on the m8-BTBT/c8-BTBT pair because the frontier orbital structure and relative position of the conjugated core is nearly identical, leading to very similar J_{ij} and $\vec{\nabla}J_{ij}$ (Figure S24a). Thus, we only have to consider changes in the directions of the phonon polarization vectors and energies when assessing the effect of chemical structure changes on $\sigma_{ij,T}$. The phonon density of states projected onto the BTBT portion of the molecule (PDOS) provides insight into the changes in phonon mode energies between c8-BTBT and m8-BTBT. In Figure S24b, we see that c8-BTBT has slightly more states at higher energy compared to lower energy than m8-BTBT. This decrease in PDOS for c8-BTBT partially explains the reduced $\sigma_{ij,T}$ (see Table 1). Thus, our results support the idea that the inclusion of side chains in BTBT-based materials “locks” the conjugated core into place and shifts phonon modes to higher energy, proposed in the work of Illig et al. [28].

On the other hand, the changes in PDOS do not fully account for the fluctuation $\sigma_{ij,T}$ in m8-BTBT being 1.5 times larger than c8-BTBT, so we must consider changes in the direction of phonon polarization vectors. Since $\vec{\nabla}J_{ij}$ is the same for c8-BTBT and m8-BTBT, any change observed in the EP coupling parameters must be due to a change in phonon polar-

ization. We verify this statement by defining a spectrum of average EP coupling parameters ($|g_{avg}(\omega)|^2$) as $B(\omega)/PDOS(\omega)$, where $B(\omega)$ is the spectral density of EP coupling from Figure 4. A detailed discussion of the calculation of the $|g_{avg}(\omega)|^2$ for all materials is contained in SI section 5. In Figure S24c, we clearly see that $|g_{avg}(\omega)|^2$ is reduced at energies $> 200 \text{ cm}^{-1}$ for c8-BTBT, which indicates that the acoustic and low-energy optic phonons are more orthogonal to $\vec{\nabla}J_{ij}$ for c8-BTBT. Therefore, the additional octyl chain on c8-BTBT changes the polarization vector directions such that the low energy phonons are more decoupled from the hole, which reduces $\sigma_{ij,T}$ and increases μ_h .

6 Transient Localization Theory

The connection between the Hamiltonian parameters and the measured mobility is a highly debated point. It was fairly soon realized that the measured mobility is too slow to be consistent with band transport (it would imply unphysically short scattering length). Many authors have adopted a variety of quantum dynamics methods to propagate the charge carrier including the coupling with nuclear modes. A theoretical framework that seems particularly useful to compare between materials has been proposed by Fratini et. al [29], and was used to construct a “map” of molecular semiconductors in ref [8]. It avoids the integration of quantum or semiclassical equations of motion, and it is based on the idea of transient localization, namely the localization of the charge due to dynamic disorder in the timescale τ_R of the fluctuation of the transfer integral. Using a Kubo-Greenwood approach and a relaxation time approximation, the mobility can be expressed in closed form as

$$\mu = \frac{e}{2k_B T} \frac{L(\tau_R)^2}{\tau_R} \quad (17)$$

The squared transient localization length $L(\tau_R)^2$ at time τ_R is the average of the same quantity computed

along the two Cartesian dimensions of the high mobility plane, i.e. $L(\tau_R)^2 = (L_{xx}(\tau_R)^2 + L_{yy}(\tau_R)^2)/2$. The transient localization length in each direction can be operatively computed (equation (18)) from the eigenstates $\{|m\rangle\}$ of a system with static disorder equivalent in magnitude to the dynamic disorder at a given temperature (in essence, a system where the nuclear modes have been frozen):

$$L_{xx}^2(\tau_R) = \frac{1}{Z} \sum_{n,m} e^{-E_n/k_B T} \left| \langle n | \hat{j}_x | m \rangle \right|^2 \frac{2}{(\hbar\tau_R^{-1})^2 + (E_m - E_n)^2} \quad (18)$$

$$\hat{j}_x = -i \sum_{k,l} (x_k - x_l) J_{kl} |k\rangle \langle l| \quad (19)$$

Where Z is the partition function and $\{x_k\}$ is the position of the localized states $\{|k\rangle\}$ used to express the eigenstates, $|n\rangle = \sum_k C_{nk} |k\rangle$. An analogous relation holds for $L_{yy}^2(\tau_R)$.

In practice, one builds a Hamiltonian for a 2D lattice of molecules where the nearest neighbor transfer integral is distributed according to a given distribution. The localization length is evaluated via equation (18) using eigenstates obtained via a repeated diagonalization of many instances of the disordered Hamiltonian. The harmonic approximation, and the approximation of a linear EP coupling imply that the distribution of the transfer integral is Gaussian is fully determined by the standard deviation $\sigma_{ij,T}$ which can be computed from the EP coupling as described above in section 5. The original theory was developed assuming a single characteristic frequency $\omega_R = \tau_R^{-1}$ for the fluctuation of the transfer integral. In a number of works, this frequency was calculated from coupled molecular dynamics/quantum chemistry calculations and appears to be fairly similar among molecular semiconductors (all within the 30-70 cm^{-1} range) [8]. It is important to notice that the computed mobility is not very sensitive to small changes in τ_R . For example, an increase (decrease) of the value of τ_R by 50% causes a decrease (increase) of the mobility of about 30%.

The detailed calculation of the EP coupling based

Table 5: Lattice parameters, relaxation times used in hole mobility calculations are displayed. Full mobility tensor values ($\mu_{xx}, \mu_{xy}, \mu_{yy}$) in the high mobility plane, and temperature dependent exponents are shown.

Material	a (Å)	b (Å)	γ (deg)	τ_R (cm ⁻¹)	μ_{xx} (cm ² V ⁻¹ s ⁻¹)	μ_{yy} (cm ² V ⁻¹ s ⁻¹)	μ_{xy}	a
c8-BTBT	6.05	7.37	90	49.3	6.68	3.03	3.04	0.972
BTBT	5.95	7.97	90	39.1	1.92	0.006	0.006	0.835
m8-BTBT	6.08	7.48	90.1	47.2	1.976	0.89	0.898	1.18
TIPS-PN	16.2	7.75	112	49.0	2.41	0.268	0.246	0.938
TES-ADT	13.7	7.22	108	64.9	7.02	1.41	1.35	1.19
TIPS-ADT	8.76	-	-	53.9	1.09	0	0	0.988

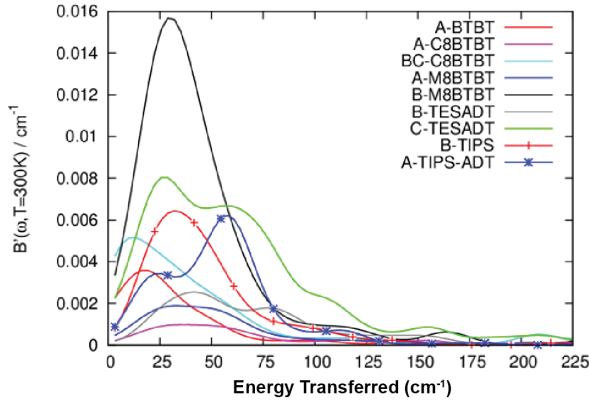


Figure S25: Spectral density weighted by the phonon population for all molecular pairs with $\sigma_{ij}, T = 300K > 200 \text{ cm}^{-1}$.

on an accurate phonon Hamiltonian seems to confirm that the characteristic fluctuation time is not changing substantially across materials. Combining equation (2) and (3) from the main text, we can define a spectral density weighted by the phonon population

$$B'_{ij}(\omega, T) = \frac{1}{2N_q} \sum_I \coth\left(\frac{\hbar\omega_I}{2k_B T}\right) |g_{ij,I}|^2 \delta(\hbar\omega - \hbar\omega_I) \quad (20)$$

This function focuses on the energy range of thermally populated phonon modes ($\hbar\omega < k_B T$), and is illustrated in Figure S25 (for $T = 300K$). It has a broad peak in the region of 10-90 cm^{-1} for all materi-

als. More quantitatively, we can evaluate an average characteristic fluctuation frequency as

$$\langle\omega_R\rangle = \frac{\int \omega B'_{ij}(\omega, T) d\omega}{\int B'_{ij}(\omega, T) d\omega}, \quad (21)$$

limiting the integration range to the “classical modes” i.e. $0 < \omega < k_B T/\hbar$. this characteristic fluctuation frequency averaged over transfer integrals present in each material has been reported for each material in Table 5, and is used to evaluate mobility.

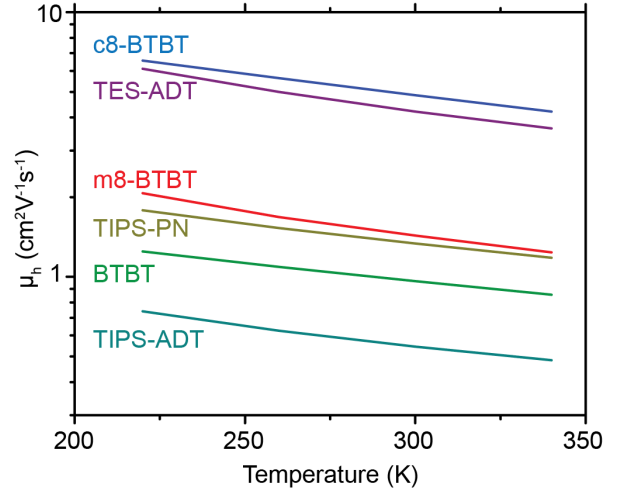


Figure S26: Temperature dependence of average μ_h for each material.

The mobilities in Table 1 of the main text have been computed considering a finite 2D lattice of 5000

sites with different realizations of disorder, and repeating the computation of equation (18) 25 times per material. The typical relative error in the computed mobility due to the finite number of systems considered is below 2%. The complete description of the anisotropic μ_h tensor is given in Table 5. This tensor was used to compute the minimum and maximum mobility values seen in Table 1 of the main text.

The temperature dependence of μ_h for each material is shown in Figure S26. Since each material is assumed to be a single crystal, μ_h decreases with increasing temperature; a characteristic of delocalized transport. Experimentally measured μ_h s for highly crystalline samples follow a power law ($\mu_h \sim T^{-a}$). Computed power law exponents are shown in Table 5.

References

- [1] W. C. Still, M. Kahn, and A. Mitra, “Rapid chromatographic technique for preparative separations with moderate resolution,” *The Journal of Organic Chemistry*, vol. 43, no. 14, pp. 2923–2925, 1978.
- [2] J. M. Adhikari, K. Vakhshouri, B. D. Calitree, A. Hexemer, M. A. Hickner, and E. D. Gomez, “Controlling crystallization to improve charge mobilities in transistors based on 2,7-dioctyl[1]benzothieno[3,2-b][1]benzothiophene,” *J. Mater. Chem. C*, vol. 3, pp. 8799–8803, 2015.
- [3] T. Izawa, E. Miyazaki, and K. Takimiya, “Molecular ordering of high-performance soluble molecular semiconductors and re-evaluation of their field-effect transistor characteristics,” *Advanced Materials*, vol. 20, no. 18, pp. 3388–3392, 2008.
- [4] V. S. Vyas, R. Gutzler, J. Nuss, K. Kern, and B. V. Lotsch, “Optical gap in herringbone and [small pi]-stacked crystals of [1]benzothieno[3,2-b]benzothiophene and its brominated derivative,” *CrystEngComm*, vol. 16, pp. 7389–7392, 2014.
- [5] J. E. Anthony, J. S. Brooks, D. L. Eaton, and S. R. Parkin, “Functionalized pentacene: improved electronic properties from control of solid-state order,” *Journal of the American Chemical Society*, vol. 123, no. 38, pp. 9482–9483, 2001.
- [6] M. M. Payne, S. R. Parkin, J. E. Anthony, C.-C. Kuo, and T. N. Jackson, “Organic field-effect transistors from solution-deposited functionalized acenes with mobilities as high as 1 cm²/Vs,” *Journal of the American Chemical Society*, vol. 127, no. 14, pp. 4986–4987, 2005.
- [7] A. K. Hailey, A. J. Petty, J. Washbourne, K. J. Thorley, S. R. Parkin, J. E. Anthony, and Y.-L. Loo, “Understanding the crystal packing and organic thin-film transistor performance in isomeric guest–host systems,” *Advanced Materials*, vol. 29, no. 23, p. 1700048, 2017.
- [8] S. Fratini, S. Ciuchi, D. Mayou, G. T. de Laisardière, and A. Troisi, “A map of high-mobility molecular semiconductors,” *Nature Materials*, vol. 16, p. 998, 2017.
- [9] J. E. Anthony, “Functionalized acenes and heteroacenes for organic electronics,” *Chemical Reviews*, vol. 106, no. 12, pp. 5028–5048, 2006.
- [10] K. Schulze, T. Bilkay, and S. Janietz, “Triisopropylsilylethynyl-functionalized anthradithiophene derivatives for solution processable organic field effect transistors,” *Applied Physics Letters*, vol. 101, no. 4, p. 043301, 2012.
- [11] P. A. Seeger, L. L. Daemen, and J. Z. Larese, “Resolution of vision, a crystal-analyzer spectrometer,” *Nuclear Instruments and Methods in Physics Research Section A: Accelerators, Spectrometers, Detectors and Associated Equipment*, vol. 604, no. 3, pp. 719 – 728, 2009.
- [12] S. F. Parker, A. J. Ramirez-Cuesta, and L. Daemen, “Vibrational spectroscopy with neutrons: Recent developments,” *Spectrochimica Acta Part A: Molecular and Biomolecular Spectroscopy*, vol. 190, pp. 518 – 523, 2018.

- [13] J. P. Perdew, K. Burke, and M. Ernzerhof, “Generalized gradient approximation made simple,” *Phys. Rev. Lett.*, vol. 77, pp. 3865–3868, 1996.
- [14] S. Grimme, “Semiempirical gga-type density functional constructed with a long-range dispersion correction,” *Journal of Computational Chemistry*, vol. 27, no. 15, pp. 1787–1799, 2006.
- [15] A. D. Becke and E. R. Johnson, “A density-functional model of the dispersion interaction,” *The Journal of Chemical Physics*, vol. 123, no. 15, p. 154101, 2005.
- [16] A. D. Becke and E. R. Johnson, “A simple effective potential for exchange,” *The Journal of Chemical Physics*, vol. 124, no. 22, p. 221101, 2006.
- [17] A. Tkatchenko and M. Scheffler, “Accurate molecular van der waals interactions from ground-state electron density and free-atom reference data,” *Phys. Rev. Lett.*, vol. 102, p. 073005, 2009.
- [18] M. Dion, H. Rydberg, E. Schröder, D. C. Langreth, and B. I. Lundqvist, “Van der waals density functional for general geometries,” *Phys. Rev. Lett.*, vol. 92, p. 246401, 2004.
- [19] A. V. Krukau, O. A. Vydrov, A. F. Izmaylov, and G. E. Scuseria, “Influence of the exchange screening parameter on the performance of screened hybrid functionals,” *The Journal of Chemical Physics*, vol. 125, no. 22, p. 224106, 2006.
- [20] A. D. Becke, “Density functional calculations of molecular bond energies,” *The Journal of Chemical Physics*, vol. 84, no. 8, pp. 4524–4529, 1986.
- [21] A. D. Becke, “Density-functional exchange-energy approximation with correct asymptotic behavior,” *Phys. Rev. A*, vol. 38, pp. 3098–3100, 1988.
- [22] J. Klimeš, D. R. Bowler, and A. Michaelides, “Chemical accuracy for the van der waals density functional,” *Journal of Physics: Condensed Matter*, vol. 22, no. 2, p. 022201, 2010.
- [23] K. Lee, E. D. Murray, L. Kong, B. I. Lundqvist, and D. C. Langreth, “Higher-accuracy van der waals density functional,” *Phys. Rev. B*, vol. 82, p. 081101, 2010.
- [24] a. D. Murray, K. Lee, and D. C. Langreth, “Investigation of exchange energy density functional accuracy for interacting molecules,” *Journal of Chemical Theory and Computation*, vol. 5, no. 10, pp. 2754–2762, 2009.
- [25] A. Togo and I. Tanaka, “First principles phonon calculations in materials science,” *Scripta Materialia*, vol. 108, pp. 1 – 5, 2015.
- [26] S. Piana, K. Lindorff-Larsen, R. M. Dirks, J. K. Salmon, R. O. Dror, and D. E. Shaw, “Evaluating the effects of cutoffs and treatment of long-range electrostatics in protein folding simulations,” *PLOS ONE*, vol. 7, no. 6, pp. 1–6, 2012.
- [27] A. Troisi and G. Orlandi, “The hole transfer in dna: calculation of electron coupling between close bases,” *Chemical Physics Letters*, vol. 344, no. 5, pp. 509 – 518, 2001.
- [28] S. Illig, A. S. Eggeman, A. Troisi, L. Jiang, C. Warwick, M. Nikolka, G. Schweicher, S. G. Yeates, Y. Henri Geerts, J. E. Anthony, and H. Sirringhaus, “Reducing dynamic disorder in small-molecule organic semiconductors by suppressing large-amplitude thermal motions,” *Nature Communications*, vol. 7, p. 10736, 2016.
- [29] S. Fratini, D. Mayou, and S. Ciuchi, “The transient localization scenario for charge transport in crystalline organic materials,” *Advanced Functional Materials*, vol. 26, no. 14, pp. 2292–2315, 2016.